STAT1- and NFAT-independent amplification of purinoceptor function integrates cellular senescence with interleukin-6 production in preadipocytes

Yasser Majeed[1], Aisha Y. Madani[1], Ahmed I. Altamimi[1], Raphael Courjaret[2], Muneera Vakayil[1,3], Samuel J. Fountain[4], Khaled Machaca[2], Nayef A. Mazloum[1, *]

[1]Department of Microbiology and Immunology, Weill Cornell Medicine-Qatar, Qatar Foundation, Doha, Qatar
[2]Department of Physiology and Biophysics, Weill Cornell Medicine-Qatar, Qatar Foundation, Doha, Qatar
[3]College of Health & Life Sciences, Hamad Bin Khalifa University, Qatar Foundation, Doha, Qatar
[4]School of Biological Sciences, University of East Anglia, Norwich, United Kingdom

*Corresponding author:

Nayef A. Mazloum (nam2016@qatar-med.cornell.edu)

Word count: 3972 (excluding Abstract/Methods/References/Figure Legends).

Data availability: All the datasets generated in the current study are available from the corresponding author upon request.

Funding statement: This publication was made possible by a National Priorities Research Program grant (NPRP10-1205-160010) awarded to NAM by the Qatar National Research Fund (QNRF) and Biomedical Research Program (BMRP) funds at Weill Cornell Medicine-Qatar (WCM-Q), a program funded by Qatar Foundation. AYM was supported by a Graduate Student Research Award (GSRA4-1-0330-17010) from QNRF. AIA was supported by an Undergraduate Research Experience Program grant (UREP25-026-3-005) awarded by QNRF and by a Student Research Mentorship Program grant (SRMP 003-01) awarded by WCM-Q.

Author contribution: YM developed the concept, designed and performed experiments, analysed and interpreted data, and wrote the manuscript. NAM provided overall supervision, and assisted YM with data interpretation and revised the manuscript. AYM, AIA, MV, and RC performed experiments or provided experimental support. SJF and KM contributed to experimental design and provided intellectual and technical inputs. All authors provided feedback on the manuscript and approved its submission.

Conflict of interest: The authors declare that they have no conflicts of interest.

Ethics approval: The Institutional Animal Care and Use Committee (IACUC) at Weill Cornell Medicine-Qatar approved all the animal experiments (Protocol 2015-0026) and the project was carried out in an AAALAC International accredited facility.

Acknowledgements: The authors acknowledge support from the imaging core facility at Weill Cornell Medicine-Qatar. We are also grateful to Ms. Cindy Conti and her team from the WCM-Q vivarium core for their assistance with the animal experiments. The core facilities are supported by a Biomedical Research Program (BMRP) grant awarded by Qatar Foundation. The authors are also grateful to Dr. Mayyasa Rammah and Dr. Isra Marei for providing reagents, MS1 VEGF angiosarcoma cells, and experimental support.

Abbreviations: AT, Adipose Tissue; cGAS, Cyclic GMP-AMP Synthase; STING, Stimulator of Interferon Genes; STAT1, Signal Transducer and Activator of Transcription 1; NFAT, Nuclear Factor of Activated T-cells; IL-6, Interleukin-6; ATP, Adenosine Triphosphate; UTP, Uridine Triphosphate; ADP, Adenosine Diphosphate; UDP, Uridine Diphosphate; Entpd, Ectonucleoside Triphosphate Diphosphohydrolase; 5'-NTE, 5'-ectonucleotidase; DDIS, DNA Damage-induced Senescence; DSB, Double-strand break; NFκB, Nuclear Factor κ B subunit; ER, Endoplasmic reticulum.

Keywords: DNA damage; senescence; purinergic signaling; inflammation; Adora3; interleukin-6.

Running title: Amplified purinoceptor function in senescence-associated inflammation.

Bullet point summary

What is already known?

- Cellular senescence is associated with the secretion of pro-inflammatory molecules such as interleukin-6.
- Signaling by extracellular nucleotides like ATP promotes inflammation and adipose tissue dysfunction in obesity.

What this study adds?

- Purinergic receptors that respond to ATP, ADP, and adenosine are robustly upregulated in senescent preadipocytes.
- Exposure of senescent preadipocytes to these agonists exacerbates inflammation by enhancing interleukin-6 secretion.

Clinical significance of the findings.

- Inhibitors targeting specific purinoceptors may curb the secretion of pro-inflammatory cytokines by senescent cells.
- These inhibitors may have therapeutic utility in conditions like aging, obesity, and cancer.

Abstract

Background and Purpose

Senescent preadipocytes promote adipose tissue dysfunction by secreting pro-inflammatory factors but little is known about the mechanisms regulating their production. We investigated if upregulated purinoceptor function sensitized senescent preadipocytes to cognate agonists and how such sensitization regulated inflammation.

Experimental Approach

Etoposide was used to trigger senescence in 3T3-L1 preadipocytes. CRISPR/Cas9 technology or pharmacology allowed studies of transcription factor function. Fura-2 imaging was used for calcium measurements. Interleukin-6 levels were quantified using quantitative PCR and ELISA. Specific agonists and antagonists supported studies of purinoceptor coupling to interleukin-6 production. Experiments in MS1 VEGF angiosarcoma cells and adipose tissue samples from obese mice complemented preadipocyte experiments.

Key Results

1. DNA damage-induced senescence robustly upregulated purinoceptor expression levels in preadipocytes and MS1 VEGF angiosarcoma cells.
2. ATP-evoked Ca^{2+} release was potentiated in senescent preadipocytes and ATP exposure enhanced interleukin-6 production, an effect mimicked by ADP but not UTP in a calcium-independent manner.
3. Senescence-associated upregulation and activation of the adenosine A3 receptor also enhanced interleukin-6 production.
4. Nucleotide hydrolysis was not essential because exposure to ATPγS also enhanced interleukin-6 secretion.
5. Pharmacological experiments suggested coupling of P2X ion channels and $P2Y_{12}$-$P2Y_{13}$ receptors to downstream interleukin-6 production.
6. Interleukin-6 signaling exacerbated inflammation during senescence and compromised adipogenesis.

Conclusions and Implications

We report a previously uncharacterized link between cellular senescence and purinergic signaling in preadipocytes and endothelial cancer cells, raising the possibility that upregulated purinoceptors play key modulatory roles in senescence-associated conditions like obesity and cancer. There is potential for exploitation of specific purinoceptor antagonists as therapeutics in inflammatory disorders.

Introduction

According to the World Health Organization, the prevalence of obesity has nearly tripled in the last half-century, and it is associated with significant morbidity and mortality (Bluher, 2019). AT performs key physiological functions, including lipid storage and secretion of adipokines like leptin (Sakers, De Siqueira, Seale & Villanueva, 2022). Although the primary functional unit of AT is the adipocyte, other key AT-resident cells include fibroblasts, macrophages, and preadipocytes, which terminally differentiate into adipocytes (Ghaben & Scherer, 2019). In contrast, obesity triggers AT dysfunction, which adversely impacts on whole-body metabolism. AT dysfunction and inflammation also contribute to Type 2 Diabetes (T2D), dyslipidemia, hypertension, and non-alcoholic fatty liver disease (NAFLD) – collectively termed 'metabolic syndrome' (Eckel, Grundy & Zimmet, 2005). Local inflammation in AT exacerbates systemic inflammation in obesity by releasing cytokines like interleukin-6 (IL-6) and tumor necrosis factor-α (TNF-α) into the circulation (Berg & Scherer, 2005). Studies also implicate the accumulation of DNA-damaged senescent cells in AT dysfunction (Tchkonia et al., 2010). Senescence is an early event in obesity and senescent preadipocytes exhibit increased glycolysis, respiration, and ATP production (Pini et al., 2021). Senescent cells also show profound epigenetic changes (Nacarelli, Liu & Zhang, 2017), are defective in proteostasis and endoplasmic reticulum (ER) stress signaling (Sabath et al., 2020), and secrete a plethora of molecules - termed as senescence-associated secretory phenotype (SASP) (Coppe, Desprez, Krtolica & Campisi, 2010). For example, the presence of cytosolic DNA in senescent preadipocytes activates the cGAS-STING pathway to stimulate STAT1-dependent production of CXCL10 (Madani et al., 2021). Conversely, deletion of STAT1 in AT improves mitochondrial function and mitigates inflammation (Cox et al., 2020). Pharmacological depletion of senescent cells rescues age-associated metabolic dysfunction (Baker et al., 2016). The pleiotropic cytokine IL-6 is a key SASP factor secreted by both mouse and human cells (Coppe, Desprez, Krtolica & Campisi, 2010), and it promotes insulin-resistance in obesity (Almuraikhy et al., 2016). Identification and pharmacological targeting of proteins that promote the SASP is interesting because it holds promise in reversing inflammation and tissue dysfunction.

ATP is an extracellular signaling nucleotide and an evolutionarily conserved Danger-Associated Molecular Pattern (DAMP) molecule, which signals via well-characterised ionotropic (P2X) and metabotropic (P2Y) purinergic receptors (Di Virgilio, Sarti & Coutinho-Silva, 2020). Although ATP is the only known agonist of P2X channels, potent agonists of G-protein-coupled P2Y receptors include adenosine diphosphate ($P2Y_1$, $P2Y_{12}$, $P2Y_{13}$), uridine triphosphate (UTP) and ATP ($P2Y_2$, $P2Y_4$), uridine diphosphate ($P2Y_6$), and UDP-sugars ($P2Y_{14}$) (Illes et al., 2021; Jacobson et al., 2020). Distinct P2Y receptors couple downstream to specific G-proteins ($G\alpha_q$, $G\alpha_s$, $G\alpha_{i/o}$) and activate signal transduction pathways including phospholipase C-dependent calcium (Ca^{2+}) release from the endoplasmic reticulum ($G\alpha_q$), and stimulation or inhibition of adenylyl cyclase by $G\alpha_s$ or $G\alpha_{i/o}$ G-proteins, respectively (Erb & Weisman, 2012). Although purinoceptors contribute to key physiological functions, they also drive metabolic dysfunction. For example, upregulated function of $P2X_7$ promotes AT inflammation (Pandolfi et al., 2015) and $P2Y_6$ signaling exacerbates obesity and insulin-resistance

(Steculorum et al., 2017). Elevated levels of extracellular ATP, ADP, and adenosine are observed in inflammation, and dynamic changes in purinergic signaling potentially drive tissue dysfunction (Campwala & Fountain, 2013; Cauwels, Rogge, Vandendriessche, Shiva & Brouckaert, 2014; Di Virgilio, Sarti & Coutinho-Silva, 2020). Little is known about the transcriptional mechanisms that regulate purinoceptor expression. NFκB signaling increased $P2Y_2$ expression in epithelial cells, and nerve injury augmented microglial expression of $P2Y_{12}$ receptors (Degagne et al., 2009; Eun, Seo, Park, Lee, Chang & Kim, 2014; Jing et al., 2019). Extracellular nucleotide levels are tightly regulated by plasma membrane-localized hydrolytic enzymes, including ectonucleoside triphosphate diphosphohydrolases (Entpd) and 5'-ectonucleotidase (5'-NTE). Entpd enzymes hydrolyze ATP and ADP to AMP while 5'-NTE converts AMP to adenosine (Yegutkin, 2008). Extracellular adenosine also activates specific purinergic P1 receptors (Adora1-3) but, unlike ATP or ADP, it performs an 'inflammation-dampening' function (Hasko, Linden, Cronstein & Pacher, 2008). There is little known about the impact of cellular DNA damage and senescence on purinergic signaling or about the effect of such an interaction on inflammation. The aim of this study was to investigate – using molecular and pharmacological approaches - if upregulated function of purinergic receptors in senescent preadipocytes sensitized them to cognate agonists and identify how such sensitization regulated senescence-associated inflammation.

Materials and methods

Cell culture:

3T3-L1 preadipocytes:
3T3-L1 preadipocytes (Cat. SP-L1-F, Zen-Bio) were cultured in a 37ºC humidified CO_2 incubator in Dulbecco's Modified Eagle Medium (DMEM; Cat. 12430-054, ThermoFisher Scientific) containing 10% calf serum (Cat. 16170-078, ThermoFisher Scientific) and 1% antibiotic-antimycotic (Cat. 15240-062, ThermoFisher Scientific) (Abdesselem et al., 2016; Majeed et al., 2021). For culture maintenance, cells were plated at a density of 250-300 x 10^3 cells in 10-cm petri dishes and sub-cultured every 3 days (with medium replenishment 2 days post-plating). Cells were used up to passage number 20 for experiments. Etoposide treatment: Typically, cells were plated in 6-well plates at a density of 100 x 10^3 cells/well and allowed a post-trypsinization recovery period of 24 hours prior to exposure to 6.25 μM etoposide (or 0.025% anhydrous DMSO) for 24 hours (in complete medium). Post-exposure, cells were incubated with fresh etoposide-free complete medium every 48 hours for the duration of the experiment. Samples were collected and analyzed at specific time-points, as exemplified by data shown in Figure 1. H_2O_2 treatment: Cells were plated in 6-well plates at a density of 200 x 10^3 cells/well and allowed a post-trypsinization recovery period of 24 hours prior to exposure to 200 μM H_2O_2 for 3 hours in complete medium. A second exposure to 200 μM H_2O_2 for 3 hours was performed 72 hours later, and samples were collected for analysis after 96 hours (Madani et al., 2021). Experiments with cyclosporin A (NFAT signaling inhibitor) and ML120B (NFκB signaling inhibitor): Cyclosporin A was used at a final concentration of 5 μg/ml (25 mg/ml stock solution) and ML120B was used at a final concentration of 10 μM (5 mM stock solution). Cells were exposed to these chemicals both during

etoposide treatment and for 24 hours post-washout. Following this 48-hour exposure, cells were collected in lysis buffer for qPCR analysis. Exposure to purinergic agonists to quantify changes in IL-6 mRNA: A typical experiment (e.g., Figure 6e) involved exposing proliferating or senescent cells to increasing concentrations (0.08 – 50 μM) of ATP, ADP, or UTP for 3 hours prior to sample collection. A similar exposure time was also used for experiments involving NECA (Figure 8c), ATPγS (Figure 8h), CGS21860 (Figure 9a), and 2CIIBMECA (Figure 9b). Experiments with 10 μM PSB0739 ($P2Y_{12}$ antagonist) and 10 μM MRS2211 ($P2Y_{13}$ inhibitor) combination, 50 μM PPADS (P2X antagonist), or 50 μM A438079 ($P2X_7$ antagonist): In these experiments, senescent cells were preincubated with the antagonist(s) for 30 minutes and it was maintained during ATP or ADP exposure, which was for 3 hours. Exposure to recombinant mouse IL-6 (Figure 9f): Following a 30-minute incubation in Opti-MEM, proliferating or senescent cells were exposed to 25 ng/ml recombinant mouse IL-6 for 5 hours (prepared in Opti-MEM; 25 μg/ml stock in 0.1% BSA/PBS) prior to sample collection for analysis.

MS1 VEGF angiosarcoma cells:
MS1 VEGF angiosarcoma cells (Cat. CRL2460) were obtained from ATCC and cultured as described previously (Majeed et al., 2019). Cells were cultured in Dulbecco's Modified Eagle Medium (Cat.12430-054, ThermoFisher Scientific) supplemented with 10% fetal bovine serum (Cat.16170-078, ThermoFisher Scientific), 1% antibiotic-antimycotic (Cat.15240-062, ThermoFisher Scientific), and 1 mM sodium pyruvate. For culture maintenance, cells were plated at a density of 300 x 10^3 cells in 10-cm petri dishes and sub-cultured every 3 days (with medium replenishment 2 days post-plating). Cells were used up to passage number 10 for experiments. The senescence-induction protocol was identical to that of 3T3-L1 preadipocytes described above.

Cell counts to generate growth-curve:
3T3-L1 preadipocytes and MS1 VEGF angiosarcoma cells were treated with etoposide or DMSO in 6-well plates as described above and cell number was quantified at the indicated time-points (Figure 1c and 3e). For counts, cells were detached using 200 μL trypsin, which was neutralized using 800 μL complete medium. Cells were gently mixed prior to quantifying the cell number using a TC20 automated cell counter (Bio-Rad). For statistical analysis, the cell count at days 2-4 was compared with that at day 1 using a Student's *t*-test. These datasets passed the D'Agostino & Pearson normality test.

Quantitative PCR:

RNA extraction, cDNA synthesis, and qPCR were performed as described previously (Majeed et al., 2021). Briefly, total RNA was isolated using the miRNeasy kit (Cat. 217004, Qiagen) or the RNeasy Mini kit (Cat. 74106, Qiagen) following the manufacturer's instructions, and a DNA digestion step was incorporated by incubating the sample with DNase I (Cat.79254, Qiagen) (RT, 15 minutes) prior to RNA elution. 500-1000 ng RNA was reverse-transcribed to cDNA using the High-Capacity RNA-to-cDNA kit (Cat. 4387406, ThermoFisher Scientific). QuantStudio6 Flex Real-Time PCR System (ThermoFisher Scientific) was used for qPCR and the thermal cycling

parameters were as follows: Stage I: Denaturation (50°C, 20 seconds; 95°C, 10 minutes); Stage II (40 cycles): 95°C, 15 seconds; 60°C, 1 minute; Stage III (Melt curve analysis): 95°C, 15 seconds; 60°C, 1 minute; 95°C, 30; seconds; 60°C, 15 seconds. Sequences of all the primers used in the study are listed in Supplementary Table 1. qPCR data were quantified using the 2^{-DDCt} method. Ribosomal Protein Lateral Stalk Subunit P0 (RPLP0) was used as the 'housekeeping' reference gene throughout, and its expression levels were stable across groups regardless of experimental manipulation.

Confocal microscopy:

DyLight™ Phalloidin 594 staining: Cells were plated in 1% w/v gelatin-coated glass-bottom 6-well or 12-well plates for imaging. Cells were washed 1x with PBS, fixed using 4% paraformaldehyde (PFA) (RT, 15 minutes), washed 3x with PBS, permeabilized with 0.25% Triton X-100 prepared in PBS (RT, 15 minutes), and washed 3x with PBS prior to staining. Cells were incubated with 3 units of DyLight™ Phalloidin 594 (300 units/ml) diluted in PBS containing 0.25% Triton X-100 (RT, 30 minutes), washed 3x with PBS, incubated with PBS containing 1 μg/ml Hoechst (RT, 10 minutes), and washed 3x with PBS prior to imaging. Fixed, independent experimental samples were labelled in one batch. Images were captured on a Carl Zeiss LSM-880 microscope using a 63x objective. A series of z-sections through each sample were collected using the 2x2 Tile Scan function. DyLight™ Phalloidin 594 and Hoechst were excited using a DPSS 561 nm and 405 nm laser, respectively. Images were analyzed using Fiji – ImageJ software (www.imagej.net/Fiji). The Z-project tool in Fiji was used to compact the z-sections and generate 2-D images for presentation.

Calcein-AM staining: Proliferating or senescent cells (days 5-7 post etoposide-washout) were plated in 1% w/v gelatin-coated glass-bottom 6-well plates for imaging. For staining, 1 mM calcein-AM solution was pre-mixed with 10% pluronic acid (1:1 ratio) and then diluted in Hank's Buffered Saline Solution containing 1.5 mM $CaCl_2$ and 1.2 mM $MgCl_2$ (HBSS/Ca^{2+}/Mg^{2+}) to give a final calcein-AM concentration of 1 μM. Cells were incubated with calcein-AM for 60 minutes in a CO_2 incubator, washed in HBSS/Ca^{2+}/Mg^{2+} for 30 minutes to allow calcein-AM de-esterification, and imaged in fresh HBSS/Ca^{2+}/Mg^{2+}. Images were captured on a Carl Zeiss LSM-880 microscope using a 63x objective. A series of z-sections through each sample were collected using the 3x3 Tile Scan function. Images were analyzed using Fiji – ImageJ software (www.imagej.net/Fiji). The Z-project tool in Fiji was used to compact the z-sections and generate 2-D images for presentation.

DNA damage-induced H2AX phosphorylation (Serine 139): 3T3-L1 preadipocytes were plated in 1% w/v gelatin-coated glass-bottom 96-well plates at a density of 5 x 10^3 cells/well. 24 hours later, they were exposed to 6.25 μM etoposide or DMSO (0.025%) for 6 hours, fixed using 4% PFA (RT, 15 minutes), washed 3x with PBS, and permeabilized using 0.25% Triton X-100 prepared in PBS (RT, 15 minutes). Non-specific antibody binding was minimized using a blocking buffer containing 5% BSA and 0.1% Tween-20 dissolved in PBS (RT, 1 hour). Fixed, independent experimental

samples were stained in one batch. The H2AX phospho-specific antibody (S139, Cat. ab2893, Abcam) was prepared in the blocking buffer at a dilution of 1:200 and incubated with the samples overnight at 4°C on a rocker. Samples were then washed 5x with PBS and incubated with a goat anti-rabbit secondary antibody (conjugated to Alexa Fluor™ 568; 1:500; 1 hour, RT) prepared in blocking buffer. Samples were washed 3x with PBS, incubated with PBS containing 1 μg/ml Hoechst (RT, 10 minutes), washed 3x with PBS, and then imaged on a Carl Zeiss LSM-880 microscope using a 100x objective. Alexa Fluor™ 568 and Hoechst were excited using a DPSS 561 nm and 405 nm laser, respectively. Images were analyzed using Fiji – ImageJ software (www.imagej.net/Fiji). The Z-project tool in Fiji was used to compact the z-sections and generate 2-D images for presentation. The experimental details provided conform with BJP guidelines (Alexander et al., 2018).

CRISPR/Cas9 technology:

We previously used CRISPR/Cas9 technology to generate stable 3T3-L1 preadipocytes lacking STAT1 (Madani et al., 2021). A single lentiviral transfer plasmid encoding the guide RNA (gRNA) and Cas9 was procured from Genscript. The gRNA sequences were GCTTTCACGGAGGTTCGACG (Scrambled^{gRNA}) and GGTCGCAAACGAGACATCAT (STAT1^{gRNA}), respectively. To generate lentiviral particles, HEK293T cells were co-transfected (using Lipofectamine 2000) with plasmids encoding STAT1^{gRNA} (10 μg) (or Scrambled^{gRNA}) and the lentiviral packaging/envelope plasmids (psPAX2 (8 μg) and MD2 (4 μg)). 6 hours later, the transfection medium was replaced with complete medium and the lentiviral supernatants were collected 48 hours post-transfection, centrifuged to clear cell debris and filter-sterilized prior to storage at -80°C. 3T3-L1 preadipocytes (passage 11-12) were incubated with lentiviral particles in the presence of polybrene (4 μg/ml) for 48 hours and passaged 2-3 times in the presence of puromycin (2 μg/ml), and validated for STAT1-deletion prior to experiments. Exposure of Control and STAT1 knockout 3T3-L1 preadipocytes to etoposide was as described above.

ATP-dependent luciferase assay:

Assays were performed using the ATP Bioluminescence Assay Kit HS II (Cat. 11699709001, Roche), according to the manufacturer's instructions. Briefly, ATP and ADP stock solutions were diluted to the appropriate concentration in PBS and aliquoted (50 μL) in a 96-well white flat-bottom plate (Costar, Cat. 3917). Real-time luminescence measurements were performed using the FlexStation^{III} 96-well plate reader. Following a short baseline measurement, 50 μL luciferase reagent was added to each well by automatic transfer with concurrent luminescence measurements. Wells containing PBS alone were used as control.

Intracellular Ca^{2+} measurements:

Standard bath solution (SBS) was used for intracellular Ca^{2+} measurement experiments performed using Fura-2 AM on the FlexStation^{III} 96-well plate reader, as described

previously (Majeed et al., 2010). The composition of SBS was as follows (in mM): 135 NaCl, 5 KCl, 1.2 $MgCl_2$, 1.5 $CaCl_2$, 8 Glucose, and 10 HEPES. pH was adjusted to 7.4 using 5M NaOH. Fura-2 AM (1 mM) and 10% pluronic acid were mixed in 1:1 ratio prior to dilution in SBS to yield a final concentration of 4 μM Fura-2 AM. Cells plated in poly-D-lysine-coated 96-well plates (Cat. 3842, Corning) were incubated with the Ca^{2+} indicator for 60 minutes in a CO_2 incubator, and washed in SBS for 30 minutes to allow dye de-esterification prior to analysis. For experiments using etoposide, 5 x 10^3 cells/well were plated in a 96-well plate, treated with 6.25 μM etoposide, and analyzed 48 hours post-etoposide washout. 5 x 10^3 proliferating cells were plated 48 hours prior to experiments in the same plate for comparison and the plate was designed such that proliferating and senescent cells were analyzed in alternating rows or columns to minimize potential time- and position-dependent artefacts on the FlexStation^{III} 96-well plate reader. Exploratory control experiments (n=3) were performed to optimize Ca^{2+} measurements experiments (Figures 6a and 7a) and to confirm an expected effect of thapsigargin (100 nM) on the ATP- and UTP-elicited Ca^{2+} signals (Figures 6d and 7d). Incubation with thapsigargin was for 30 minutes during the wash step.

Analysis of lean *versus* obese mice:

The Institutional Animal Care and Use Committee (IACUC) at Weill Cornell Medicine-Qatar approved all the animal experiments (Protocol 2015-0026) and the project was carried out in an AAALAC International accredited facility. Mice were housed at 23°C in plastic, single-use, individually ventilated cages (Innovive, USA) with unrestricted access to food and water, and maintained in a 12-h light, 12-h dark cycle (Lights on 0600 hrs.; lights off 1800 hrs.). For the diet-induced obesity studies, 13-week-old male C57BL/6J mice were fed a high-fat diet (HFD) consisting of 60 Kcal% fat (Research Diets, Cat. D12492) or Chow (Pico-Vac Lab Rodent Diet, Cat. 5061) for 20 weeks prior to sacrifice. Mice were randomly assigned to Chow or HFD groups. The investigator could not be blinded to these groups because of the obvious obese phenotype evident in mice that were fed HFD. Mice were euthanized using CO_2 asphyxia and dissected using sterile instruments to isolate epididymal white adipose tissue (eWAT) and liver. Tissues were immediately snap-frozen in liquid N_2 and stored at -80°C until analysis. To prepare the stromal vascular fraction (SVF), eWAT was digested in a buffer containing 8 mg/ml Collagenase D and 3 units/ml Dispase II for 30 minutes at 37°C with gentle agitation on a shaker. The preparation was centrifuged, and the pellet was washed 3x with warm complete medium prior to re-suspension and plating in 6-well plates. To remove red blood cells (RBC), medium was gently removed after 3 hours, followed by 1x PBS wash before medium replenishment. Cells were collected in Qiazol (Cat. 79306, Qiagen) after overnight incubation and used for qPCR analysis. Qiazol was also used as the lysis buffer when homogenizing eWAT and liver tissues to extract total RNA. Animal data reported in this study comply with the ARRIVE guidelines (Kilkenny, Browne, Cuthill, Emerson, Altman & Group, 2010).

3T3-L1 preadipocyte differentiation:

3T3-L1 preadipocytes were differentiated to adipocytes, as previously described (Abdesselem et al., 2016; Majeed et al., 2021). For differentiation experiments, cells were plated in 6-well plates at a density of 200 x 10^3/well. Medium was replaced 2 days post-plating, followed by incubation with the differentiation cocktail 48 hours later. Cells were incubated with the differentiation cocktail for 2 days then switched to post-differentiation medium, which was replenished every 2 days for the duration of the experiment. The differentiation cocktail was prepared in DMEM supplemented with 10% fetal bovine serum (FBS), 10 μg/ml insulin, 0.5 mM 3-isobutyl-1-methylxanthine (IBMX) and 1 μM dexamethasone. Post-differentiation medium contained 10% FBS and 10 μg/ml insulin. For experiments with recombinant mouse IL-6, cells were treated with 25 ng/ml IL-6 2 days prior to differentiation and then every 2 days until samples were collected for analysis (Differentiation Day 6).

IL-6 Enzyme-Linked Immunosorbent Assay (ELISA):

IL-6 concentration in cell culture supernatants was measured using the mouse IL-6 Quantikine ELISA kit (Cat. M6000B, R&D Systems), according to the manufacturer's instructions. Proliferating or senescent preadipocytes were exposed to purinergic agonists for 8 hours prior to the collection of supernatants, which were centrifuged at 1200 rpm (4°C) to clear cell debris, aliquoted, and stored at -80°C. In all experiments, IL-6 standards were included (7–500 pg/ml) to construct a standard curve and calculate sample IL-6 concentration based on absorbance. Samples were diluted 1:1 in RDI-14 assay buffer, as recommended. Absorbance measurements were performed on a CLARIOstar plate-reader (BMG Labtech) and absorbance @540 nm was subtracted from absorbance @450 nm for all samples. A standard curve was fitted by linear regression method in GraphPad Prism using the absorbance values of IL-6 standards.

Chemicals:

Etoposide - Cat. 2200 (Cell Signaling Technology); DyLight™ Phalloidin 594 - Cat. 12877 (Cell Signaling Technology); ML120B - Cat. 4899 (Tocris); Cyclosporin A – Cat. 9973 (Cell Signaling Technology); Adenosine Triphosphate – Cat. A2383 (Sigma-Aldrich); Adenosine Diphosphate – Cat. A2754 (Sigma-Aldrich); Uridine Triphosphate – Cat. 94370 (Sigma-Aldrich); N-ethylcarboxamidoadenosine (NECA) – Cat. 1691 (Tocris); CGS21680 – Cat. 1063 (Tocris); 2CIIBMECA – Cat. 1104 (Tocris); ATPγS – Cat. 4080 (Tocris); Fura-2 AM – Cat. F1221 (ThermoFisher Scientific); Thapsigargin – Cat. 12758 (Cell Signaling Technology); PSB0739 – Cat. 3983 (Tocris); MRS2211 – Cat. 2402 (Tocris); PPADS – Cat. 0625 (Tocris); A438079 – Cat. 2972 (Tocris); Recombinant mouse IL-6 – Cat. RMIL6 (Invitrogen); Insulin – Cat. I9278 (Sigma-Aldrich); 3-isobutyl-1-methylxanthine (IBMX) – Cat. PHZ1124 (Gibco); Dexamethasone – Cat. D1756 (Sigma-Aldrich); Calcein-AM – Cat. C3099 (ThermoFisher Scientific).

Data and analysis:

Studies were designed to generate experimental groups of equal size and all data points were included in the analysis. When experiments were performed in 6-well plates, controls and treatments were regularly randomized between experiments to improve robustness. In intracellular Ca^{2+} measurements, the 96-well plate was designed such that control and test samples were analyzed in alternating columns and rows to minimize potential artefacts on the plate reader. Experiments could not be blinded because of personnel limitations. We did not conduct any sample size estimations because the effect size could not be predicted given that many of the experiments had not been previously performed. Intracellular Ca^{2+} measurement data are presented as n/N, where n is the number of independent experiments and N is the total number of biological replicates. qPCR data were analysed by normalising data for test groups to a control group and, for experiments of this type, the y-axis indicates fold matched control values (indicated throughout in the figure legends). Data were analyzed using GraphPad Prism 9.0 and are presented as mean ± SEM. For statistical analysis of experiments comparing 2 groups, an unpaired Student's *t*-test or Wilcoxon matched-pairs signed rank test was used. In experiments that included >2 groups and in which the test groups were statistically compared to a control that was normalized to 1, the non-parametric Kruskal-Wallis test with post hoc Dunn's test was used. In all other cases, Analysis of Variance (ANOVA) with Tukey's post hoc test was used. In multigroup studies with parametric variables, post hoc tests were conducted only if F achieved $P<0.05$ and there was no significant variance inhomogeneity. For all statistical analysis, a 'p' value of <0.05 was considered statistically significant and analysis was only performed on independent experiments (n=5-6). All datasets that were quantified and subjected to statistical analysis were generated from at least 5 independent experiments. The specific experimental 'n' is indicated in the figure legends and in all cases the indicated 'n' is the number of independent values on which statistical analysis was done. The manuscript complies with BJP's recommendations and requirements on experimental design and analysis (Curtis et al., 2018).

Results:

DNA damage-induced senescence (DDIS) in 3T3-L1 preadipocytes.

We established a cellular model of DNA damage-induced senescence (DDIS) by exposing 3T3-L1 preadipocytes to a low concentration of etoposide (6.25 μM) for 24 hours, followed by a 'washout' period (Figure 1a). Etoposide induces DNA double-strand breaks (DSBs) by inhibiting DNA topoisomerase II (Walles, Zhou & Liliemark, 1996). DSBs generated by a 6-hour exposure to etoposide (but not DMSO) induced phosphorylation of histone H2AX at serine 139, indicated by the appearance of DNA-damage foci (Figure 1b and supplementary figure 1a). Etoposide-treated cells showed characteristics of senescence, including growth-arrest, upregulation of cyclin-dependent kinase inhibitor 1A (p21), increased senescence-associated β-galactosidase activity, cellular enlargement, and transcriptional induction of SASP molecules. In contrast to proliferating preadipocytes, nuclei in senescent cells showed abnormalities including

multinucleation, presence of micronuclei, and 'blebbing'. However, robust conversion of calcein-AM to its fluorescent metabolite suggested that they were metabolically active (Figure 1c-f and supplementary figure 1b, c). DNA damage also triggered the induction of pro-inflammatory cytokines such as IL-6 and IL-1β. Interleukin expression was induced within 24 hours of DNA-damage and remained high throughout senescence (Figure 1g and supplementary figure 1d).

Upregulation of metabotropic and ionotropic purinergic P2 receptors in DNA-damaged, senescent preadipocytes.

To assess potential changes in purinergic signaling in DDIS, we compared mRNA levels of metabotropic (P2Y) and ionotropic (P2X) receptors in proliferating *versus* senescent preadipocytes. Importantly, expression of all 7 mouse P2Y receptors was significantly induced during senescence (Figure 2a and supplementary figure 2a). Expression levels of $P2Y_1$, $P2Y_2$, $P2Y_{12}$ and $P2Y_{13}$ were increased within 6-24 hours of DNA damage. In contrast, $P2Y_4$, $P2Y_6$, and $P2Y_{14}$ receptors showed slower induction, increasing in expression 24 hours after washout ($P2Y_4$ and $P2Y_{14}$) or later ($P2Y_6$) (Figure 2a and supplementary figure 2a). Among P2X channels, levels of P2X1, $P2X_3$, $P2X_6$, and $P2X_7$ were significantly increased in senescent preadipocytes, while those of $P2X_4$ and $P2X_5$ were significantly downregulated (Figure 2b and supplementary figure 2b). We next assessed changes in purinoceptor expression in preadipocytes induced to senesce using 200 μM hydrogen peroxide (H_2O_2) (Madani et al., 2021), which revealed upregulation of $P2Y_1$, $P2Y_2$, $P2Y_4$, $P2Y_6$, $P2Y_{12}$, $P2Y_{13}$, and $P2Y_{14}$ (Figure 3a, b).

To assess possible *in vivo* relevance to obesity, we compared P2Y expression in epididymal white adipose tissue (eWAT) and stromal vascular fraction (SVF) isolated from lean or obese mice. In eWAT isolated from obese mice *versus* lean, we observed increased expression of $P2Y_2$ and $P2Y_6$; $P2Y_{13}$ levels were lower and there were no differences in $P2Y_1$, $P2Y_{12}$, or $P2Y_{14}$ levels. However, in SVF isolated from eWAT, expression levels of $P2Y_6$, $P2Y_{12}$, $P2Y_{13}$, and $P2Y_{14}$ were all significantly higher in samples from obese mice (Figure 3c, d). To explore if our findings in eWAT were relevant to other metabolically important tissues, we quantified expression levels of purinergic receptors in liver samples. In contrast to eWAT, analysis of liver tissue revealed no increase in expression levels of $P2Y_1$, $P2Y_2$, $P2Y_4$, $P2Y_6$, $P2Y_{12}$, $P2Y_{13}$, or $P2Y_{14}$ when comparing obese mice *versus* lean (Supplementary figure 3a). These data suggested that obesity in mice was associated with higher eWAT expression levels of select purinoceptors.

Upregulation of purinergic P2 receptors in senescent MS1 VEGF angiosarcoma cells.

DNA damage, senescence, and SASP are biologically important features of cancer (Sieben, Sturmlechner, van de Sluis & van Deursen, 2018). Importantly, high concentrations of purinergic agonists such as ATP are found in the tumor microenvironment, and data suggest that targeting this pathway strongly modulates both the host and tumor response (Di Virgilio & Adinolfi, 2017). Therefore, we speculated that upregulated purinoceptor function in cancer cells may be an important

functional component. To this end, we established a DDIS model in MS1 VEGF angiosarcoma cells, which are cancerous pancreatic endothelial cells that form tumors resembling human angiosarcomas in nude mice (Arbiser et al., 2000). Exposure to 6.25 μM etoposide triggered senescence in MS1 VEGF angiosarcoma cells, characterized by growth-arrest, upregulation of p21 and IL-6, and cellular enlargement. However, the cells were metabolically active (Figure 3e-h and supplementary figure 3b, c). Importantly, senescent MS1 VEGF angiosarcoma cells expressed significantly higher mRNA levels of all P2Y receptors (except $P2Y_2$) (Figure 3i).

Collectively, our data suggested that the upregulation of purinergic receptors was a response to DNA damage in both preadipocytes and cancer cells, which raised the possibility that their activity regulated key aspects of DDIS and inflammation.

Upregulation of P2Y receptors in DNA-damaged preadipocytes is largely independent of STAT1, NFAT, or NFκB activation.

To gain insights into the transcriptional program(s) promoting purinoceptor-induction in DDIS, we genetically or pharmacologically inhibited the activity of 3 key transcription factors whose activity is linked to DNA damage – STAT1, NFAT, and NFκB (Gabriel et al., 2016; Janssens & Tschopp, 2006; Madani et al., 2021). Using previously established STAT1 knockout (KO) 3T3-L1 preadipocytes (Madani et al., 2021), we discovered that while DNA damage-dependent induction of interferon-β (IFN-β) was suppressed by STAT1-deletion, the increase in expression levels of P2Y receptors was largely unaffected. Among P2X channels, only $P2X_3$ upregulation was significantly blunted in DNA-damaged STAT1 KO preadipocytes (Figure 4a and supplementary figure 4). Next, we used the calcineurin inhibitor cyclosporin A to assess if NFAT signaling promoted purinoceptor-induction (Boss, Abbott, Wang, Pavlath & Murphy, 1998). Exposure of 3T3-L1 preadipocytes to 5 μg/ml cyclosporin A during DNA damage-induction significantly suppressed CXCL10 induction but it was largely ineffective at preventing the increase in purinoceptor expression (Figure 4b and supplementary figure 5). Finally, we also used the IκK2-selective inhibitor ML120B to assess the impact of NFκB-inhibition on purinoceptor expression (Nagashima et al., 2006). Exposure of 3T3-L1 preadipocytes to 10 μM ML120B significantly suppressed CXCL10 induction driven by DNA damage, but it failed to prevent the increase in P2X channels or P2Y receptor expression (Figure 5 and supplementary figure 6). In summary, these experiments suggested that STAT1, NFAT, or NFκB signaling was engaged during DDIS to stimulate IFN-β or CXCL10 production but was largely dispensable for purinoceptor-induction.

Exposure to extracellular ATP enhanced IL-6 production in senescent 3T3-L1 preadipocytes.

To directly investigate if upregulation of P2 receptor mRNA levels translated to changes in protein function, we performed experiments using adenosine triphosphate (ATP), which activates P2X channels and $P2Y_2$ and $P2Y_4$ receptors. Application of extracellular ATP (10-100 μM) elicited rapid and concentration-dependent Ca^{2+} signals in proliferating 3T3-L1 preadipocytes that were abolished by pretreatment with 100 nM

thapsigargin, which depletes ER Ca^{2+} stores (preliminary data; n=3). Importantly, ATP-elicited Ca^{2+} signals were significantly potentiated during DDIS (Figure 6a-d). To explore the functional importance of sensitization of senescent preadipocytes to extracellular ATP, we focused on the pro-inflammatory cytokine IL-6 for the following reasons. First, IL-6 exacerbates obesity-associated AT dysfunction (Almuraikhy et al., 2016). Second, its expression levels were induced in our cellular models of DDIS and a link between purinergic signaling and IL-6 expression has been previously reported (Kountz, Jairaman, Kountz, Stauderman, Schleimer & Prakriya, 2021). Third, autocrine and paracrine actions of secreted IL-6 modulate the inflammatory milieu in obesity (Berg & Scherer, 2005). Therefore, we compared the effect of ATP exposure on IL-6 expression in proliferating and senescent preadipocytes. Importantly, in contrast to proliferating preadipocytes, exposure of senescent preadipocytes to ATP produced a concentration-dependent increase in IL-6 mRNA levels and enhanced IL-6 secretion (Figure 6e, f). These data suggested functional coupling of ATP-activated purinoceptors to IL-6 production in DDIS, with a possible link to potentiated ER Ca^{2+} release.

ADP, but not UTP, increased IL-6 production in senescent preadipocytes without eliciting Ca^{2+} signals.

To dissect the functional coupling between purinergic receptors and IL-6 production, we next assessed the effects of uridine triphosphate (UTP) and adenosine diphosphate (ADP), which – unlike ATP - do not activate P2X channels and show high selectivity towards cognate P2Y receptors. For example, both UTP and ATP are agonists of $P2Y_2$ and $P2Y_4$ receptors, which trigger ER Ca^{2+} release via coupling to $G_{q/11}$ G-proteins and phospholipase C (PLC) (Jacobson et al., 2020). Because ATP exposure potentiated ER Ca^{2+} release in senescent preadipocytes, we speculated that UTP exposure may elicit a similar response. Therefore, we evaluated the effects of exposing proliferating and senescent preadipocytes to UTP. Like ATP, exposure to extracellular UTP (10-100 μM) elicited transient and concentration-dependent Ca^{2+} signals in proliferating 3T3-L1 preadipocytes that were abolished by thapsigargin (preliminary data; n=3). UTP-elicited Ca^{2+} signals were significantly potentiated during DDIS (Figure 7a-d). However, in stark contrast to ATP, exposure to UTP did not enhance IL-6 expression in senescent preadipocytes (Figure 7e). Extracellular ADP activates $P2Y_1$, $P2Y_{12}$, and $P2Y_{13}$ receptors and, among these, the $P2Y_1$ receptor engages $G_{q/11}$ G-proteins and phospholipase C (PLC) (Jacobson et al., 2020). Therefore, we compared the action of ADP with ATP and UTP. Importantly, extracellular ADP failed to elicit Ca^{2+} signals but robustly increased IL-6 production in senescent preadipocytes but not in proliferating cells (Figure 7f-i). To rule out contamination of the ADP preparation with ATP, we tested both chemicals using an ATP-dependent luciferase assay. ATP (10-50 μM) significantly increased luciferase activity in a concentration-dependent manner (Figure 7j, k). However, luciferase activity was not enhanced by either PBS or ADP (10-50 μM). Collectively, these data suggested that ATP and ADP triggered IL-6 production by senescent preadipocytes and that an increase in cytosolic Ca^{2+} was dispensable for this effect.

Purinergic P1 and P2 receptors are both coupled to IL-6 production in senescent preadipocytes.

The concentrations of extracellular purine nucleotides are tightly regulated via hydrolysis by ectonucleoside triphosphate diphosphohydrolases (Entpd) and 5'-ectonucleotidase (5'-NTE) to adenosine monophosphate (AMP) and adenosine, respectively (Figure 8a). Based on our observation that both ATP and ADP augmented IL-6 production in DDIS, we hypothesized that this effect may be explained by their hydrolysis to adenosine, followed by downstream activation of P1 receptors. To test this idea, we quantified changes in the expression levels of Entpd1-3 and 5'-NTE genes during DDIS. Etoposide-induced DNA damage triggered a rapid (within 24 hours) and sustained increase in Entpd1, Entpd3, and 5'-NTE levels. In contrast, Entpd2 levels were similar between senescent and proliferating preadipocytes (Figure 8b and supplementary figure 7). To test if adenosine receptor activation could recapitulate the effects of ATP and ADP on IL-6 production, we exposed proliferating and senescent preadipocytes to the stable adenosine analog N-ethylcarboxamidoadenosine (NECA) (25-50 μM). Interestingly, in contrast to proliferating cells, exposure of senescent preadipocytes to NECA significantly enhanced IL-6 secretion (Figure 8c, d). Further, mRNA levels of adenosine receptors Adora2a and Adora3 were significantly induced in senescent preadipocytes. Adora1 was not reliably detected and Adora 2b expression was unchanged during DDIS (Figure 8e and supplementary figure 7). NECA did not elicit Ca^{2+} signals in proliferating or senescent preadipocytes, unlike ATP (Figure 8f). We further hypothesized that if hydrolysis of ATP/ADP to adenosine was essential to induce IL-6, then this effect should be blunted if ATP hydrolysis was impaired. Therefore, we performed experiments using the non-hydrolysable ATP analog, ATPγS. As expected, application of ATPγS (50 μM) elicited robust Ca^{2+} signals, which were significantly potentiated in senescent 3T3-L1 preadipocytes (Figure 8g). However, surprisingly, ATPγS (25-50 μM) also robustly enhanced IL-6 production, an effect similar in amplitude to ATP and ADP (Figure 8h-k). These data suggested that hydrolysis of purine nucleotides to adenosine was not required to augment IL-6 production and that both P1 and P2 receptors were functionally coupled to IL-6 production in senescent preadipocytes.

Receptor-coupling to IL-6 production and detrimental effects on preadipocyte function.

We next used a pharmacological approach to identify the purinergic receptors whose activation was coupled to IL-6 production in DDIS. First, we exploited the availability of highly specific Adora2b and Adora3 agonists – CGS21860 and 2CIIBMECA, respectively – to identify the specific P1 receptor subtype (Borea, Gessi, Merighi, Vincenzi & Varani, 2018). Exposure to 2CIIBMECA, but not to CGS21860, enhanced IL-6 expression in senescent 3T3-L1 preadipocytes. However, 2CIIBMECA was not as effective as NECA (Figure 9a, b). Selective inhibition of $P2Y_{12}$ and $P2Y_{13}$ by PSB0739 and MRS2211, respectively, has been previously reported (Micklewright, Layhadi & Fountain, 2018) and combined inhibition of $P2Y_{12}$ and $P2Y_{13}$ using 10 μM each of PSB0739 and MRS2211 abolished the ADP-induced increase in IL-6 expression (Figure 9c). The previously reported non-selective P2X inhibitor PPADS (50 μM) (Jacques-Silva

et al., 2010), but not the $P2X_7$ inhibitor A438079 (50 μM) (Trang, Schmalzing, Muller & Markwardt, 2020), significantly blunted the ATP-induced increase in IL-6 expression in senescent preadipocytes (Figure 9d, e). Finally, to explore autocrine/paracrine IL-6 signaling in our DDIS model, we exposed proliferating and senescent 3T3-L1 preadipocytes to recombinant mouse IL-6. Exposure to extracellular IL-6 (25 ng/ml) robustly increased IL-6 expression suggesting autoregulation, and expression levels of 2 key pro-inflammatory cytokines – IL-1β and IL-4 – were also enhanced by IL-6 exposure in senescent cells (Figure 9f). Further, 3T3-L1 adipogenesis experiments revealed that IL-6 exposure significantly reduced expression levels of leptin, fatty acid synthase (Fas), and stearoyl-CoA desaturase-1 and 2 (SCD1/2) (Figure 9g, h). Collectively, these experiments suggested that activation of Adora3, $P2Y_{12}$, $P2Y_{13}$, and P2X channels by their specific agonists was functionally linked downstream to IL-6 production in senescent preadipocytes (Figure 10).

Discussion:

We report that senescence amplifies the function of several purinergic P1 and P2 receptors and activation of some of these receptors (e.g., Adora3, P2X, $P2Y_{12}$, $P2Y_{13}$) augments the production of IL-6, with little dependence on Ca^{2+} signaling. To our knowledge, exacerbation of DDIS and inflammation by amplified purinergic signaling has not been previously revealed. In contrast, a protective effect of $P2Y_{14}$ receptor activation *against* senescence in hematopoietic stem cells was reported (Cho et al., 2014). The transcriptional mechanisms underlying the increase in purinoceptor expression are unclear. Future studies could investigate the involvement of p53 because it is a DNA damage response (DDR) pathway component (Vaddavalli & Schumacher, 2022), and transcriptional regulation of some purinoceptors by p53 is known (Gruenbacher et al., 2019; Molle, Arguin, Jemfer, Placet, Dagenais Bellefeuille & Gendron, 2020; Urano et al., 1997). The DDR is a complex program that engages cell cycle regulators, tissue-remodeling and ER stress factors, and antiapoptotic molecules (Hernandez-Segura, Nehme & Demaria, 2018; Kang et al., 2015). STAT1 is a key effector protein engaged by the cGAS-STING cytosolic DNA-sensing pathway (Madani et al., 2021). We therefore investigated if it could drive purinoceptor expression in senescence. However, our experiments using STAT1 KO preadipocytes revealed no effect of STAT1-deletion on purinoceptor-induction. Further, although both senescent 3T3-L1 preadipocytes and MS1 VEGF angiosarcoma cells overexpressed purinergic receptors, cytosolic DNA micronuclei were only apparent in preadipocytes, which again suggests that cGAS-STING-STAT1 signaling may not be involved. We also observed differential kinetics of purinoceptor induction - rapid (e.g., $P2Y_2$), semi-rapid (e.g., $P2Y_1$, $P2Y_{12}$ and $P2Y_{13}$) and 'delayed' (e.g., $P2Y_6$, $P2X_3$ and $P2X_7$) - which suggests that more than one transcription factor regulates purinoceptor levels during DDIS.

The underlying molecular pathways activated by etoposide and H_2O_2 to promote purinoceptor expression may be common. Importantly, some P2Y receptors were expressed at higher levels in SVF isolated from obese mice. This result suggests relevance to obesity but it may not indicate an *increase* in mRNA in preadipocytes. Instead, this may be explained by obesity-induced infiltration of eWAT by immune cells,

which robustly express purinoceptors. Purification of adipocyte progenitors from eWAT followed by molecular analysis may provide direct measurements of changes in purinoceptor levels. Upregulation of purinoceptors in senescent MS1 VEGF angiosarcoma cells suggests relevance to cancer (Sieben, Sturmlechner, van de Sluis & van Deursen, 2018), which could be explored further by injecting senescent, purinoceptor-overexpressing cells into nude mice followed by exposure to agonists. An important question is whether cellular ATP release is enhanced during DDIS. Although ATP is typically released by dying cells (Zanoni et al., 2022), and our protocol minimized cytotoxicity, changes in extracellular ATP levels during DDIS could be assessed. However, because Entpd1, Entpd3, and 5'-NTE are induced during DDIS, these assays may require the inclusion of Entpd inhibitors (e.g., ARL67156) (Yegutkin, 2008).

Our data suggest functional coupling of upregulated P2 (e.g., P2X, $P2Y_{12}$, $P2Y_{13}$) and P1 receptors (e.g., Adora3) to IL-6 production by senescent 3T3-L1 preadipocytes. Potentiation of ER Ca^{2+} release by ATP and UTP also suggests that the increase in $P2Y_2$ and $P2Y_4$ mRNA correlated with increased protein levels. However, we found that these 2 receptors were not coupled downstream to IL-6 production, so their precise function(s) in DDIS is unclear. The selective $P2Y_2$ inhibitor AR-C 118925XX (Ali, Turner & Fountain, 2018) will be useful to study $P2Y_2$ function in senescence. Unfortunately, specific $P2Y_4$ inhibitors are unavailable so these investigations will rely heavily on molecular approaches. Similarly, the precise functions of upregulated $P2Y_6$ and $P2Y_{14}$ receptors may be investigated by exposing cells to UDP and UDP-glucose, respectively. Although extracellular ATP and UTP both elicited ER Ca^{2+} release, only ATP increased IL-6 production. Such differential effects of ATP and UTP have been reported. Kountz et al. reported that ATP, but not UTP, induced IL-6 expression, whereas both agonists upregulated prostaglandin E2 (PGE_2) in epithelial cells (Kountz, Jairaman, Kountz, Stauderman, Schleimer & Prakriya, 2021). PGE_2 synthesis by ATP required $P2Y_2$ signaling but that of IL-6 required P2X ion channels, consistent with our data showing coupling of $P2X_1$, $P2X_3$ or $P2X_6$ to ATP-induced IL-6 secretion in DDIS. $P2X_7$ isoform switching contributes to inflammation in irradiation-induced senescence (Zhang et al., 2019). We used 'low' concentrations of ATP (≤50 μM), which minimizes $P2X_7$ activation. Moreover, the $P2X_7$ inhibitor A438079 failed to reverse the stimulatory effect on IL-6 even when 1 mM ATP was used. Together, these results argue against a major function of $P2X_7$ as a regulator of IL-6 production in DDIS. A confounding issue concerning P2X involvement is that thapsigargin abolished the Ca^{2+} signals elicited by ATP (≤50 μM), which cannot be reconciled with P2X-dependent Ca^{2+} entry. Therefore, it may be better to study P2X-dependent Ca^{2+} entry using specific inhibitors (e.g., NF449) to circumvent non-specific effects of thapsigargin on Ca^{2+} handling. We considered experiments in Ca^{2+}-free extracellular solution but these experiments were not feasible due to technical limitations with the FlexStation^{III} plate-reader, which collects data column-by-column thereby potentially causing ER Ca^{2+} store-depletion in cells incubated in Ca^{2+}-free solution.

Our pharmacological data suggest that the activation of P2X channels, $P2Y_{12}$ and $P2Y_{13}$ receptors, or Adora3 receptor stimulates IL-6 production in senescent preadipocytes. However, the downstream signal transduction events triggered by receptor activation

are unclear. The effects of ADP and NECA are Ca^{2+}-independent, so the involvement of $G_{\alpha s}$ and $G_{i/o}$ G-proteins could be speculated. However, data suggest specific coupling of $P2Y_{12}$, $P2Y_{13}$, and Adora3 to $G_{i/o}$ G-proteins (Hasko, Linden, Cronstein & Pacher, 2008; Jacobson et al., 2020), which makes this G-protein class a likely downstream transducer. The $G_{i/o}$ inhibitor, pertussis toxin, may clarify this aspect. Adora2a and 2b receptor activation promotes IL-6 secretion (Dai, Zhang, Wen, Zhang, Kellems & Xia, 2011; Ouyang et al., 2013) but we discovered a role for Adora3 function in DDIS. There is little known about the pathophysiological functions of Adora3 receptor even though a specific agonist (2CIIBMECA) and an antagonist (MRS1220) are available. The modified nucleoside N^6-methyladenosine (m^6A) was also recently identified as a high-affinity endogenous Adora3 agonist relevant to allergy and inflammation (Ogawa et al., 2021). Therefore, novel insights into Adora3 biology may be obtained by studying this receptor's function in DDIS. Our data raise the possibility that specific purinergic receptor inhibitors could potentially limit senescence-associated inflammation and may therefore have utility as therapeutics in conditions like aging, obesity, and cancer. There is existing evidence indicating that ligands targeting purinergic signaling exert anti-inflammatory effects and some of these small molecules are currently being assessed for clinical utility (Antonioli, Blandizzi, Pacher & Hasko, 2019).

In summary, we discovered that DNA damage and senescence were associated with upregulation of key purinergic P1 and P2 receptors, which were coupled to downstream production of IL-6. The discovery of this previously uncharacterized link between cellular DNA damage and purinergic signaling in preadipocytes and angiosarcomas highlights the possible relevance of this pathway to obesity-associated adipose tissue dysfunction and to cancer.

Figure Legends:

Figure 1: Etoposide-induced DNA double-strand breaks (DSBs) induce senescence and inflammation in preadipocytes. (a) Schematic of experimental design indicating etoposide-exposure and washout durations in 3T3-L1 preadipocytes. (b) Representative images of preadipocytes treated with 0.025% DMSO or 6.25 μM etoposide for 6 hours prior to staining with Hoechst and an antibody specific for histone H2AX phosphorylation at serine 139 (γH2AX) (n=5). Scale bar, 50 μm. Additional images are shown in Supplementary figure 1a. (c) Cell count data generated from proliferating (DMSO) or DNA-damaged preadipocytes (Eto) over the indicated time-course (n=5). Cells were treated with 6.25 μM etoposide or 0.025% DMSO. Inset shows changes in the expression levels of p21 mRNA quantified 3 days after etoposide-washout (n=6) (ns *vs* day 1; $P<0.05$ *vs* day 1). (d) Representative images of proliferating or senescent preadipocytes stained with X-gal to monitor activity of senescence-associated β-galactosidase (n=5). Scale bar, 1000 μm. (e) Representative images of proliferating or senescent preadipocytes stained with Hoechst and DyLight™ 594 phalloidin. Nuclei are pseudo-colored yellow for clarity. Arrows indicate signs of nuclear fragmentation (n=5). Scale bar, 100 μm. Additional images are shown in Supplementary figure 1b. (f) Representative images of proliferating or senescent preadipocytes showing calcein fluorescence (n=5). Scale bar, 100 μm. Additional

images are shown in Supplementary figure 1c. (g) qPCR data quantifying changes in the expression levels of key interleukins in proliferating or etoposide-treated preadipocytes. Etoposide exposure and washout durations are indicated in hours (h) or days (d) (n=6). Numbers on the Y-axis show fold matched control (Prolif.) values. Ct values for the dataset shown in (g) that were used for fold-change calculations are included in Supplementary figure 1d. Statistical analysis was performed using Student's *t*-test (c, growth curve), Wilcoxon matched-pairs signed rank test (c, p21 data), or Kruskal-Wallis test with post-hoc Dunn's test (g) ('ns', not significant *vs* Proliferating).

Figure 2: Upregulation of metabotropic and ionotropic purinergic P2 receptors in DNA-damaged, senescent preadipocytes. Data were generated by qPCR using RNA isolated from proliferating (Prolif.) or DNA-damaged (Etoposide) 3T3-L1 preadipocytes. Numbers on the Y-axis show fold matched control (Prolif.) values. Etoposide-exposure and washout durations are indicated in hours (h) or days (d). (a) Gene-expression analysis of G-protein-coupled (metabotropic) purinergic P2Y receptors (n=6). (b) Gene-expression analysis of ionotropic purinergic P2X receptors (n=6). The inset schematics show plasma membrane (PM) topology of P2Y (a) or P2X (b) receptors. Ct values for the dataset shown in (a) and (b) that were used for fold-change calculations are included in Supplementary figure 2. Statistical analysis was performed using Kruskal-Wallis test with post-hoc Dunn's test ('ns', not significant *vs* Proliferating).

Figure 3: Upregulation of P2Y receptors in oxidative stress-induced senescence and in senescent MS1 VEGF angiosarcoma cells. (a) Representative images of proliferating or H_2O_2-treated 3T3-L1 preadipocytes stained with X-gal to monitor activity of senescence-associated beta-galactosidase. Cells were exposed to 200 μM H_2O_2 as described in the methods (n=5). Scale bar, 1000 μm. (b) qPCR data quantifying changes in the expression levels of P2Y receptors in proliferating (Prolif.) cells or those induced to senesce (Senesc.) by exposure to H_2O_2 (n=6). Numbers on the Y-axis show fold matched control (Prolif.) values. (c) Gene-expression analysis of P2Y receptors in epididymal fat tissue (eWAT) isolated from lean or obese mice (n=6 mice per group). (d) Gene-expression analysis of P2Y receptors in stromal vascular fraction (SVF) samples prepared by enzymatic digestion of eWAT isolated from lean or obese mice (n=6 mice per group). (e) Cell count data generated from proliferating (DMSO) or DNA-damaged (Eto.) MS1 VEGF angiosarcoma cells over the indicated time-course (n=5) (ns *vs* day 1; $P<0.05$ *vs* day 1). (f, g) Representative images of proliferating or senescent MS1 VEGF angiosarcoma cells stained using DyLight™ 594 phalloidin and Hoechst (f) or Calcein-AM (g) (n=5). Scale bars, 100 μm. Additional images are shown in Supplementary figure 3b and c. (h, i) qPCR data quantifying changes in the expression levels of the indicated genes in proliferating or senescent MS1 VEGF angiosarcoma cells (n=6). Numbers on the Y-axis show fold matched control (Prolif.) values. Statistical analysis was performed using Student's *t*-test (c, d, e) or Wilcoxon matched-pairs signed rank test (b, h, i) ('ns', not significant *vs* respective control).

Figure 4: Upregulation of P2 receptors in DNA-damaged preadipocytes is largely independent of STAT1 and NFAT signaling. (a) qPCR data showing changes in the expression levels of purinergic P2 receptors in DNA-damaged control (WT) or STAT1

knockout (KO) 3T3-L1 preadipocytes (n=6). STAT1 KO preadipocytes were generated using CRISPR/Cas9 technology as previously described (see methods). Changes in the expression levels of IFN-β were monitored as a positive control. (b) qPCR data showing changes in the expression levels of purinergic P2 receptors in DNA-damaged preadipocytes exposed to solvent (Ctrl, DMSO) or 5 µg/ml cyclosporin A (NFAT inh.), which inhibits calcineurin to prevent dephosphorylation and nuclear translocation of NFAT (n=6). Changes in the expression levels of CXCL10 were monitored as a positive control. The data shown in (a) and (b) are for DNA-damaged preadipocytes i.e., exposed to etoposide. Data for proliferating preadipocytes is shown in Supplementary figures 4 and 5. Statistical analysis was performed using Student's *t*-test ('ns', not significant *vs* respective control).

Figure 5: Upregulation of P2 receptors in DNA-damaged preadipocytes is largely independent of NFκB activity. (a) qPCR data showing changes in the expression levels of purinergic P2 receptors in DNA-damaged preadipocytes exposed to solvent (Ctrl, DMSO) or 10 µM ML120B (NFκB inh.) (n=6), which inhibits IκK2 kinase to prevent nuclear translocation of NFκB. Changes in the expression levels of CXCL10 were monitored as a positive control. The data shown are for DNA-damaged preadipocytes i.e., exposed to etoposide. Data for proliferating preadipocytes is shown in Supplementary figure 6. Statistical analysis was performed using Student's *t*-test ('ns', not significant *vs* respective control).

Figure 6: Exposure to ATP enhances IL-6 production in senescent 3T3-L1 preadipocytes. (a) Intracellular Ca^{2+} measurement data showing changes in Fura-2 fluorescence triggered by exposure to the indicated concentrations of ATP or solvent (H_2O, Ctrl). Experiments were performed in extracellular Ca^{2+}-containing solution. The horizontal bar indicates the time-point at which reagents were applied (n/N=3/9). (b, c) Intracellular Ca^{2+} measurement data comparing the Ca^{2+} response elicited by ATP in proliferating or senescent preadipocytes (b) and mean data for this type of experiment (c) (n/N=5/15). (d) Intracellular Ca^{2+} measurement data showing the effect of exposure to 100 nM thapsigargin (Tg) on the Ca^{2+} signals elicited by ATP in proliferating (Prolif.) or senescent preadipocytes (n/N=3/15). (e) qPCR data showing changes in the expression levels of interleukin-6 (IL-6) in proliferating or senescent preadipocytes after a 3-hour exposure to ATP (n=6) ($P<0.05$ *vs* respective control). Numbers on the Y-axis show fold matched control (Proliferating, 0 ATP) values. (f) ELISA results quantifying IL-6 concentrations in cell culture supernatants collected from proliferating or senescent preadipocytes after an 8-hour exposure to 50 µM ATP. Cells not exposed to ATP were used as Controls (Ctrl.) (n=6) ('n.d.', not detected). Statistical analysis was performed using Student's *t*-test (c, f) or Kruskal-Wallis test with post-hoc Dunn's test (e).

Figure 7: ADP, but not UTP, enhances IL-6 production in senescent preadipocytes without eliciting calcium signals. (a) Intracellular Ca^{2+} measurement data showing changes in Fura-2 fluorescence triggered by exposure to the indicated concentrations of UTP or solvent (H_2O, Ctrl). Experiments were performed in extracellular Ca^{2+}-containing solution. The horizontal bar indicates the time-point at which reagents were applied (n/N=3/9). (b, c) Intracellular Ca^{2+} measurement data comparing the Ca^{2+} response

elicited by UTP in proliferating or senescent preadipocytes (b) and mean data for this type of experiment (c) (n/N=5/15). (d) Intracellular Ca^{2+} measurement data showing the effect of exposure to 100 nM thapsigargin (Tg) on the Ca^{2+} signals elicited by UTP in proliferating (Prolif.) or senescent preadipocytes (n/N=3/15). (e) qPCR data quantifying changes in the expression levels of interleukin-6 (IL-6) in proliferating or senescent preadipocytes after a 3-hour exposure to UTP (n=6). Numbers on the Y-axis show fold matched control (Proliferating, 0 UTP) values. (f, g) Intracellular Ca^{2+} measurement data showing changes in Fura-2 fluorescence triggered by exposure to the indicated concentrations of ADP in proliferating or senescent preadipocytes (n/N=3/15). Experiments were performed in extracellular Ca^{2+}-containing solution. The horizontal bar indicates the time-point at which reagents were applied. (h) qPCR data quantifying changes in the expression levels of interleukin-6 (IL-6) in proliferating or senescent preadipocytes after a 3-hour exposure to ADP (n=6) ($P<0.05$ *vs* respective control). Numbers on the Y-axis show fold matched control (Proliferating, 0 ADP) values. (i) ELISA results quantifying IL-6 concentrations in cell culture supernatants collected from proliferating or senescent preadipocytes after an 8-hour exposure to 50 μM ADP. Cells not exposed to ADP were used as Controls (Ctrl.) (n=6). (j, k) Data from an ATP-dependent luciferase activity assay showing changes in luminescence produced by the addition of phosphate buffered saline (PBS), ATP, or ADP at the indicated concentrations (j) and mean data for this type of experiment (k) (n/N=5/9). Statistical analysis was performed using Student's *t*-test (c, i, k) or Kruskal-Wallis test with post-hoc Dunn's test (h).

Figure 8: Purinergic P1 and P2 receptors are both coupled to IL-6 production in senescent preadipocytes. (a) Schematic showing plasma membrane (PM)-localized enzymatic components of purine nucleotide metabolism, including Ectonucleoside triphosphate diphosphohydrolases 1-3 (Entpd1-3) and Ecto-5'-nucleotidase (5'-NTE). (b) Data showing changes in the expression levels of Entpd1-3 and 5'-NTE genes in proliferating (Prolif.) or etoposide (Eto)-treated preadipocytes. Etoposide exposure and washout durations are indicated in hours (h) or days (d) (n=6). Numbers on the Y-axis show fold matched control (Prolif.) values. (c) Effect of a 3-hour exposure to 25 or 50 μM N-ethylcarboxamidoadenosine (NECA) on the expression levels of IL-6 in proliferating (Prolif.) or senescent (Senesc.) preadipocytes (n=6). Numbers on the Y-axis show fold matched control (Prolif.) values. (d) ELISA results quantifying IL-6 concentrations in cell culture supernatants collected from senescent preadipocytes after an 8-hour exposure to 50 μM NECA (n=6). (e) Data showing changes in the expression levels of adenosine receptors 2a, 2b and 3 in proliferating (Prolif.) or etoposide (Eto)-treated preadipocytes (n=6). Adora1 could not be reliably detected in either group. Numbers on the Y-axis show fold matched control (Prolif.) values. (f, g) Intracellular Ca^{2+} measurement data showing changes in Fura-2 fluorescence triggered by exposure to 50 μM ATP or NECA (f) or ATPγS (g) in proliferating or senescent preadipocytes (n/N=5/13 each for f and g). (h) Effect of a 3-hour exposure to 25 or 50 μM ATPγS on the expression levels of IL-6 in proliferating (Prolif.) or senescent (Senesc.) preadipocytes (n=6). Numbers on the Y-axis show fold matched control (Prolif.) values. (i) ELISA results quantifying IL-6 concentrations in cell culture supernatants collected from senescent preadipocytes after an 8-hour exposure to 50 μM ATPγS (n=6). (j, k)

Effect of a 3-hour exposure to 50 μM ATP (j) or ADP (k) on the expression levels of IL-6 in proliferating (Prolif.) or senescent (Senesc.) preadipocytes (n=6). Numbers on the Y-axis show fold matched control (Prolif.) values. Ct values for the dataset shown in (b) and (e) that were used for fold-change calculations are included in Supplementary figure 7. Statistical analysis was performed using Kruskal-Wallis test with post-hoc Dunn's test (b, c, e, h, j, k) or Student's *t*-test (d, i) ('ns', not significant *vs* respective control).

Figure 9: Receptor-coupling to IL-6 production and detrimental effects on inflammation and adipogenesis. (a-f) Data were generated by gene-expression analysis. (a, b) Changes in IL-6 mRNA levels in senescent preadipocytes after a 3-hour exposure to 25 μM each of the Adora2a-specific agonist CGS21860, Adora3-specific agonist 2CIIBMECA, or NECA (n=6). (c) Effect of pre-incubation with a combination of $P2Y_{12}$ inhibitor (PSB0739) and $P2Y_{13}$ inhibitor (MRS2211) on IL-6 induction triggered by exposure to 10 μM ADP in senescent preadipocytes. Both inhibitors were used at 10 μM (n=5). (d, e) Effect of pre-incubation with the P2X inhibitor PPADS (50 μM) or the $P2X_7$ inhibitor A438079 (50 μM) on IL-6 induction triggered by exposure to 50 μM ATP (d) or 1 mM ATP (e) in senescent preadipocytes (n=6). (f) qPCR data quantifying changes in the expression levels of the indicated genes after exposure to 25 ng/ml recombinant mouse IL-6 in proliferating or senescent preadipocytes (n=6). Numbers on the Y-axis show fold matched control (Proliferating) values. (g, h) Experimental data generated from adipogenesis experiments performed in the absence (Control) or presence (+IL-6) of 25 ng/ml recombinant IL-6 (g). Representative Oil Red O staining images of adipocytes (g) (scale bar, 200 μm) and qPCR data quantifying changes in the levels of the indicated genes after IL-6 treatment (n=6) (h). Numbers on the Y-axis show fold matched control values. Statistical analysis was performed using one-way ANOVA with post-hoc Tukey's test (a-e), Kruskal-Wallis test with post-hoc Dunn's test (f), or Wilcoxon matched-pairs signed rank test (h) ('ns', not significant *vs* respective control).

Figure 10: Schematic highlighting the main discovery and hypotheses related to signaling mechanisms activated downstream of purinoceptor-engagement. (a) Healthy preadipocytes express low levels of purinergic receptors and are relatively insensitive to purinergic agonists in an inflammatory context. (b, c) Senescent preadipocytes robustly upregulate many purinergic P1 and P2 receptors, which sensitizes them such that exposure to agonists such as ATP, ADP, and 2CIIBMECA potentiates IL-6 secretion downstream of receptor activation. IL-6 not only promotes its own expression but also induces IL-1β and IL-4 in senescent preadipocytes. (d) Adipocytes differentiated in the presence of IL-6 are inflamed and express lower levels of the adipokine leptin and molecules related to fatty acid synthesis. Coupling of extracellular agonists such as ADP and 2CIIBMECA to IL-6 secretion is independent of Ca^{2+} signaling and is likely mediated by G-proteins of the $G_{i/o}$ subfamily. The functional effects of IL-6 are likely through the activation of STAT3.

References

Abdesselem H, Madani A, Hani A, Al-Noubi M, Goswami N, Ben Hamidane H*, et al.* (2016). SIRT1 Limits Adipocyte Hyperplasia through c-Myc Inhibition. J Biol Chem 291**:** 2119-2135.

Alexander SPH, Roberts RE, Broughton BRS, Sobey CG, George CH, Stanford SC*, et al.* (2018). Goals and practicalities of immunoblotting and immunohistochemistry: A guide for submission to the British Journal of Pharmacology. Br J Pharmacol 175**:** 407-411.

Ali SB, Turner JJO, & Fountain SJ (2018). Constitutive P2Y2 receptor activity regulates basal lipolysis in human adipocytes. J Cell Sci 131.

Almuraikhy S, Kafienah W, Bashah M, Diboun I, Jaganjac M, Al-Khelaifi F*, et al.* (2016). Interleukin-6 induces impairment in human subcutaneous adipogenesis in obesity-associated insulin resistance. Diabetologia 59**:** 2406-2416.

Antonioli L, Blandizzi C, Pacher P, & Hasko G (2019). The Purinergic System as a Pharmacological Target for the Treatment of Immune-Mediated Inflammatory Diseases. Pharmacol Rev 71**:** 345-382.

Arbiser JL, Larsson H, Claesson-Welsh L, Bai X, LaMontagne K, Weiss SW*, et al.* (2000). Overexpression of VEGF 121 in immortalized endothelial cells causes conversion to slowly growing angiosarcoma and high level expression of the VEGF receptors VEGFR-1 and VEGFR-2 in vivo. Am J Pathol 156**:** 1469-1476.

Baker DJ, Childs BG, Durik M, Wijers ME, Sieben CJ, Zhong J*, et al.* (2016). Naturally occurring p16(Ink4a)-positive cells shorten healthy lifespan. Nature 530**:** 184-189.

Berg AH, & Scherer PE (2005). Adipose tissue, inflammation, and cardiovascular disease. Circ Res 96**:** 939-949.

Bluher M (2019). Obesity: global epidemiology and pathogenesis. Nat Rev Endocrinol 15**:** 288-298.

Borea PA, Gessi S, Merighi S, Vincenzi F, & Varani K (2018). Pharmacology of Adenosine Receptors: The State of the Art. Physiol Rev 98**:** 1591-1625.

Boss V, Abbott KL, Wang XF, Pavlath GK, & Murphy TJ (1998). The cyclosporin A-sensitive nuclear factor of activated T cells (NFAT) proteins are expressed in vascular smooth muscle cells. Differential localization of NFAT isoforms and induction of NFAT-mediated transcription by phospholipase C-coupled cell surface receptors. J Biol Chem 273**:** 19664-19671.

Campwala H, & Fountain SJ (2013). Constitutive and agonist stimulated ATP secretion in leukocytes. Commun Integr Biol 6**:** e23631.

Cauwels A, Rogge E, Vandendriessche B, Shiva S, & Brouckaert P (2014). Extracellular ATP drives systemic inflammation, tissue damage and mortality. Cell Death Dis 5**:** e1102.

Cho J, Yusuf R, Kook S, Attar E, Lee D, Park B*, et al.* (2014). Purinergic P2Y(1)(4) receptor modulates stress-induced hematopoietic stem/progenitor cell senescence. J Clin Invest 124**:** 3159-3171.

Coppe JP, Desprez PY, Krtolica A, & Campisi J (2010). The senescence-associated secretory phenotype: the dark side of tumor suppression. Annu Rev Pathol 5**:** 99-118.

Cox AR, Chernis N, Bader DA, Saha PK, Masschelin PM, Felix JB*, et al.* (2020). STAT1 Dissociates Adipose Tissue Inflammation From Insulin Sensitivity in Obesity. Diabetes 69**:** 2630-2641.

Curtis MJ, Alexander S, Cirino G, Docherty JR, George CH, Giembycz MA*, et al.* (2018). Experimental design and analysis and their reporting II: updated and simplified guidance for authors and peer reviewers. Br J Pharmacol 175**:** 987-993.

Dai Y, Zhang W, Wen J, Zhang Y, Kellems RE, & Xia Y (2011). A2B adenosine receptor-mediated induction of IL-6 promotes CKD. J Am Soc Nephrol 22**:** 890-901.

Degagne E, Grbic DM, Dupuis AA, Lavoie EG, Langlois C, Jain N*, et al.* (2009). P2Y2 receptor transcription is increased by NF-kappa B and stimulates cyclooxygenase-2 expression and PGE2 released by intestinal epithelial cells. J Immunol 183**:** 4521-4529.

Di Virgilio F, & Adinolfi E (2017). Extracellular purines, purinergic receptors and tumor growth. Oncogene 36**:** 293-303.

Di Virgilio F, Sarti AC, & Coutinho-Silva R (2020). Purinergic signaling, DAMPs, and inflammation. Am J Physiol Cell Physiol 318**:** C832-C835.

Eckel RH, Grundy SM, & Zimmet PZ (2005). The metabolic syndrome. Lancet 365**:** 1415-1428.

Erb L, & Weisman GA (2012). Coupling of P2Y receptors to G proteins and other signaling pathways. Wiley Interdiscip Rev Membr Transp Signal 1**:** 789-803.

Eun SY, Seo J, Park SW, Lee JH, Chang KC, & Kim HJ (2014). LPS potentiates nucleotide-induced inflammatory gene expression in macrophages via the upregulation of P2Y2 receptor. Int Immunopharmacol 18**:** 270-276.

Gabriel CH, Gross F, Karl M, Stephanowitz H, Hennig AF, Weber M*, et al.* (2016). Identification of Novel Nuclear Factor of Activated T Cell (NFAT)-associated Proteins in T Cells. J Biol Chem 291**:** 24172-24187.

Ghaben AL, & Scherer PE (2019). Adipogenesis and metabolic health. Nat Rev Mol Cell Biol 20**:** 242-258.

Gruenbacher G, Gander H, Rahm A, Dobler G, Drasche A, Troppmair J*, et al.* (2019). The Human G Protein-Coupled ATP Receptor P2Y11 Is Associated With IL-10 Driven Macrophage Differentiation. Front Immunol 10**:** 1870.

Hasko G, Linden J, Cronstein B, & Pacher P (2008). Adenosine receptors: therapeutic aspects for inflammatory and immune diseases. Nat Rev Drug Discov 7**:** 759-770.

Hernandez-Segura A, Nehme J, & Demaria M (2018). Hallmarks of Cellular Senescence. Trends Cell Biol 28**:** 436-453.

Illes P, Muller CE, Jacobson KA, Grutter T, Nicke A, Fountain SJ*, et al.* (2021). Update of P2X receptor properties and their pharmacology: IUPHAR Review 30. Br J Pharmacol 178**:** 489-514.

Jacobson KA, Delicado EG, Gachet C, Kennedy C, von Kugelgen I, Li B*, et al.* (2020). Update of P2Y receptor pharmacology: IUPHAR Review 27. Br J Pharmacol 177**:** 2413-2433.

Jacques-Silva MC, Correa-Medina M, Cabrera O, Rodriguez-Diaz R, Makeeva N, Fachado A*, et al.* (2010). ATP-gated P2X3 receptors constitute a positive autocrine signal for insulin release in the human pancreatic beta cell. Proc Natl Acad Sci U S A 107**:** 6465-6470.

Janssens S, & Tschopp J (2006). Signals from within: the DNA-damage-induced NF-kappaB response. Cell Death Differ 13**:** 773-784.

Jing F, Zhang Y, Long T, He W, Qin G, Zhang D*, et al.* (2019). P2Y12 receptor mediates microglial activation via RhoA/ROCK pathway in the trigeminal nucleus caudalis in a mouse model of chronic migraine. J Neuroinflammation 16**:** 217.

Kang C, Xu Q, Martin TD, Li MZ, Demaria M, Aron L*, et al.* (2015). The DNA damage response induces inflammation and senescence by inhibiting autophagy of GATA4. Science 349**:** aaa5612.

Kilkenny C, Browne W, Cuthill IC, Emerson M, Altman DG, & Group NCRRGW (2010). Animal research: reporting in vivo experiments: the ARRIVE guidelines. Br J Pharmacol 160**:** 1577-1579.

Kountz TS, Jairaman A, Kountz CD, Stauderman KA, Schleimer RP, & Prakriya M (2021). Differential Regulation of ATP- and UTP-Evoked Prostaglandin E2 and IL-6 Production from Human Airway Epithelial Cells. J Immunol 207**:** 1275-1287.

Madani AY, Majeed Y, Abdesselem HB, Agha MV, Vakayil M, Sukhun NKA*, et al.* (2021). Signal Transducer and Activator of Transcription 3 (STAT3) Suppresses STAT1/Interferon Signaling Pathway and Inflammation in Senescent Preadipocytes. Antioxidants (Basel) 10.

Majeed Y, Agarwal AK, Naylor J, Seymour VA, Jiang S, Muraki K*, et al.* (2010). Cis-isomerism and other chemical requirements of steroidal agonists and partial agonists acting at TRPM3 channels. Br J Pharmacol 161**:** 430-441.

Majeed Y, Halabi N, Madani AY, Engelke R, Bhagwat AM, Abdesselem H*, et al.* (2021). SIRT1 promotes lipid metabolism and mitochondrial biogenesis in adipocytes and coordinates adipogenesis by targeting key enzymatic pathways. Sci Rep 11**:** 8177.

Majeed Y, Upadhyay R, Alhousseiny S, Taha T, Musthak A, Shaheen Y*, et al.* (2019). Potent and PPARalpha-independent anti-proliferative action of the hypolipidemic drug fenofibrate in VEGF-dependent angiosarcomas in vitro. Sci Rep 9**:** 6316.

Micklewright JJ, Layhadi JA, & Fountain SJ (2018). P2Y12 receptor modulation of ADP-evoked intracellular Ca(2+) signalling in THP-1 human monocytic cells. Br J Pharmacol 175**:** 2483-2491.

Molle CM, Arguin G, Jemfer C, Placet M, Dagenais Bellefeuille S, & Gendron FP (2020). The expression of the P2Y6 receptor is regulated at the transcriptional level by p53. Biochem Biophys Res Commun 524**:** 798-802.

Nacarelli T, Liu P, & Zhang R (2017). Epigenetic Basis of Cellular Senescence and Its Implications in Aging. Genes (Basel) 8.

Nagashima K, Sasseville VG, Wen D, Bielecki A, Yang H, Simpson C*, et al.* (2006). Rapid TNFR1-dependent lymphocyte depletion in vivo with a selective chemical inhibitor of IKKbeta. Blood 107**:** 4266-4273.

Ogawa A, Nagiri C, Shihoya W, Inoue A, Kawakami K, Hiratsuka S*, et al.* (2021). N(6)-methyladenosine (m(6)A) is an endogenous A3 adenosine receptor ligand. Mol Cell 81**:** 659-674 e657.

Ouyang X, Ghani A, Malik A, Wilder T, Colegio OR, Flavell RA*, et al.* (2013). Adenosine is required for sustained inflammasome activation via the A(2)A receptor and the HIF-1alpha pathway. Nat Commun 4**:** 2909.

Pandolfi J, Ferraro A, Lerner M, Serrano JR, Dueck A, Fainboim L*, et al.* (2015). Purinergic signaling modulates human visceral adipose inflammatory responses: implications in metabolically unhealthy obesity. J Leukoc Biol 97**:** 941-949.

Pini M, Czibik G, Sawaki D, Mezdari Z, Braud L, Delmont T*, et al.* (2021). Adipose tissue senescence is mediated by increased ATP content after a short-term high-fat diet exposure. Aging Cell 20**:** e13421.

Sabath N, Levy-Adam F, Younis A, Rozales K, Meller A, Hadar S*, et al.* (2020). Cellular proteostasis decline in human senescence. Proc Natl Acad Sci U S A 117**:** 31902-31913.

Sakers A, De Siqueira MK, Seale P, & Villanueva CJ (2022). Adipose-tissue plasticity in health and disease. Cell 185**:** 419-446.

Sieben CJ, Sturmlechner I, van de Sluis B, & van Deursen JM (2018). Two-Step Senescence-Focused Cancer Therapies. Trends Cell Biol 28**:** 723-737.

Steculorum SM, Timper K, Engstrom Ruud L, Evers N, Paeger L, Bremser S*, et al.* (2017). Inhibition of P2Y6 Signaling in AgRP Neurons Reduces Food Intake and Improves Systemic Insulin Sensitivity in Obesity. Cell Rep 18**:** 1587-1597.

Tchkonia T, Morbeck DE, Von Zglinicki T, Van Deursen J, Lustgarten J, Scrable H*, et al.* (2010). Fat tissue, aging, and cellular senescence. Aging Cell 9**:** 667-684.

Trang M, Schmalzing G, Muller CE, & Markwardt F (2020). Dissection of P2X4 and P2X7 Receptor Current Components in BV-2 Microglia. Int J Mol Sci 21.

Urano T, Nishimori H, Han H, Furuhata T, Kimura Y, Nakamura Y*, et al.* (1997). Cloning of P2XM, a novel human P2X receptor gene regulated by p53. Cancer Res 57**:** 3281-3287.

Vaddavalli PL, & Schumacher B (2022). The p53 network: cellular and systemic DNA damage responses in cancer and aging. Trends Genet 38**:** 598-612.

Walles SA, Zhou R, & Liliemark E (1996). DNA damage induced by etoposide; a comparison of two different methods for determination of strand breaks in DNA. Cancer Lett 105**:** 153-159.

Yegutkin GG (2008). Nucleotide- and nucleoside-converting ectoenzymes: Important modulators of purinergic signalling cascade. Biochim Biophys Acta 1783**:** 673-694.

Zanoni M, Sarti AC, Zamagni A, Cortesi M, Pignatta S, Arienti C*, et al.* (2022). Irradiation causes senescence, ATP release, and P2X7 receptor isoform switch in glioblastoma. Cell Death Dis 13**:** 80.

Zhang C, Yan Y, He H, Wang L, Zhang N, Zhang J*, et al.* (2019). IFN-stimulated P2Y13 protects mice from viral infection by suppressing the cAMP/EPAC1 signaling pathway. J Mol Cell Biol 11**:** 395-407.

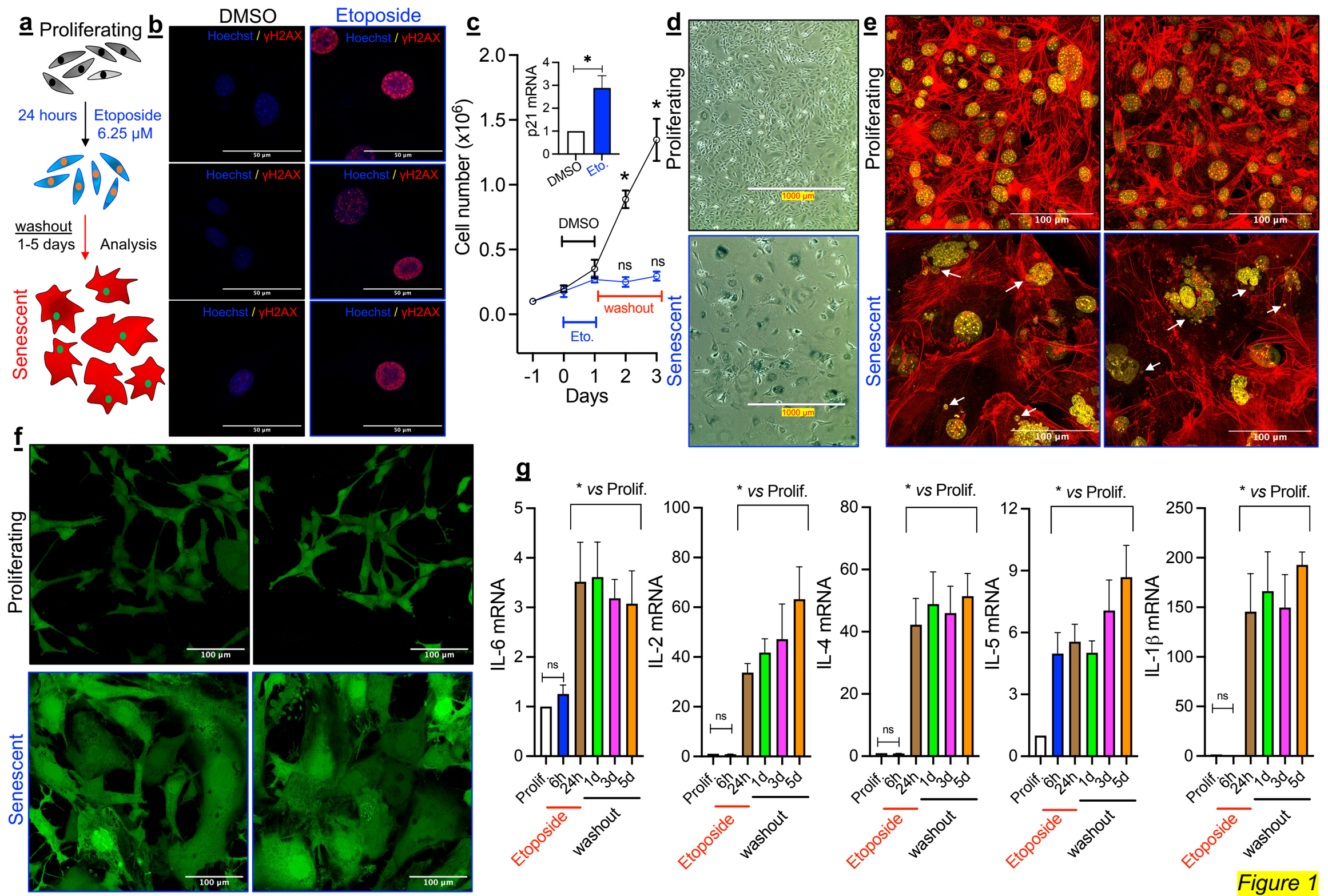
a Proliferating
24 hours
Etoposide 6.25 µM
washout 1-5 days
Analysis
Senescent
b
DMSO
Etoposide
Hoechst / γH2AX
50 µm
c
Cell number (x10^6)
Days
DMSO
Eto.
washout
ns
p21 mRNA
d
Proliferating
Senescent
1000 µm
e
100 µm
f
g
* vs Prolif.
IL-6 mRNA
IL-2 mRNA
IL-4 mRNA
IL-5 mRNA
IL-1β mRNA
Prolif.
6h
24h
1d
3d
5d
Etoposide
washout

Figure 1

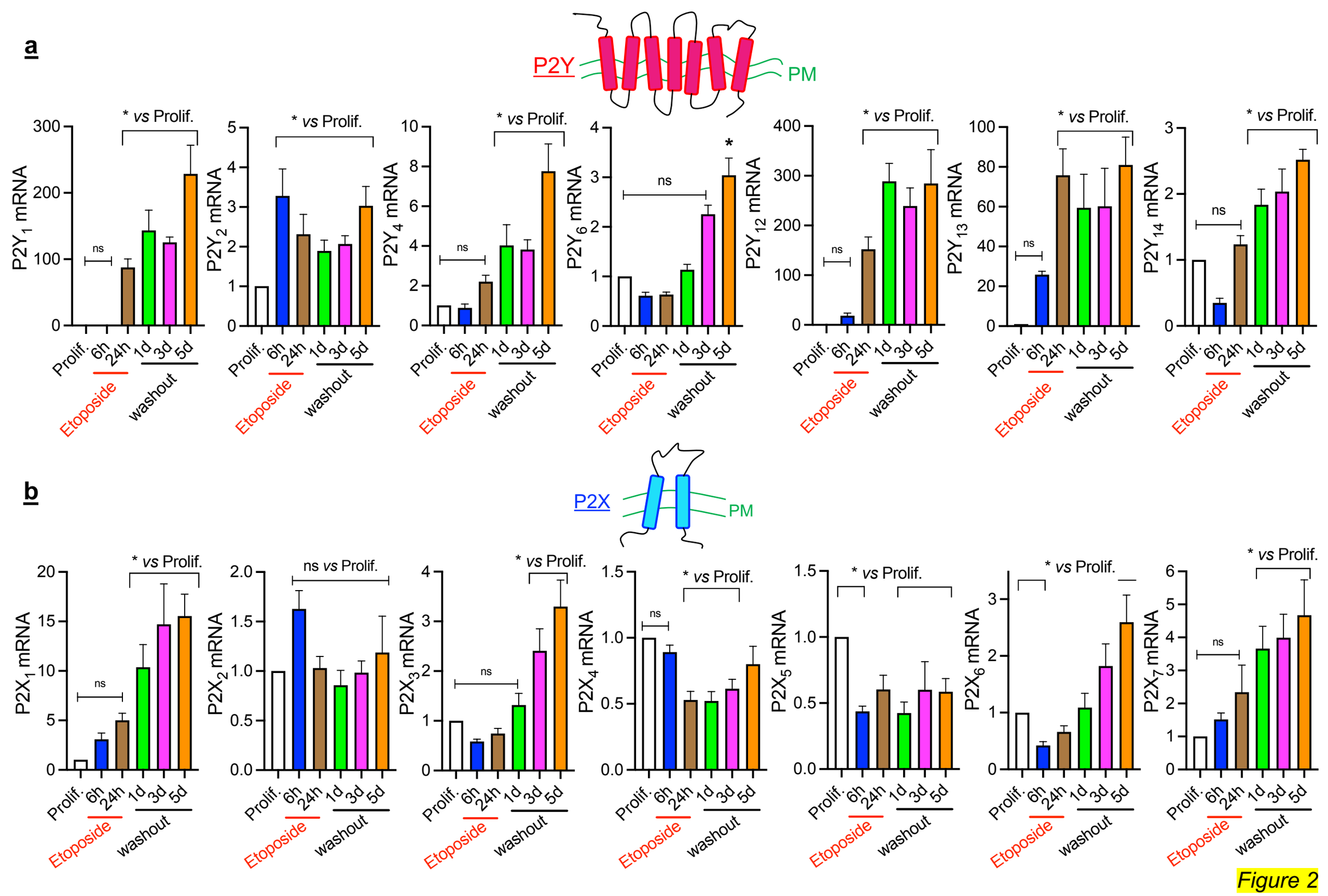
a
P2Y
PM
P2Y1 mRNA
P2Y2 mRNA
P2Y4 mRNA
P2Y6 mRNA
P2Y12 mRNA
P2Y13 mRNA
P2Y14 mRNA
* vs Prolif.
ns
*
Prolif.
6h
24h
1d
3d
5d
Etoposide
washout
b
P2X
PM
P2X1 mRNA
P2X2 mRNA
P2X3 mRNA
P2X4 mRNA
P2X5 mRNA
P2X6 mRNA
P2X7 mRNA
* vs Prolif.
ns vs Prolif.
ns
Prolif.
6h
24h
1d
3d
5d
Etoposide
washout

Figure 2

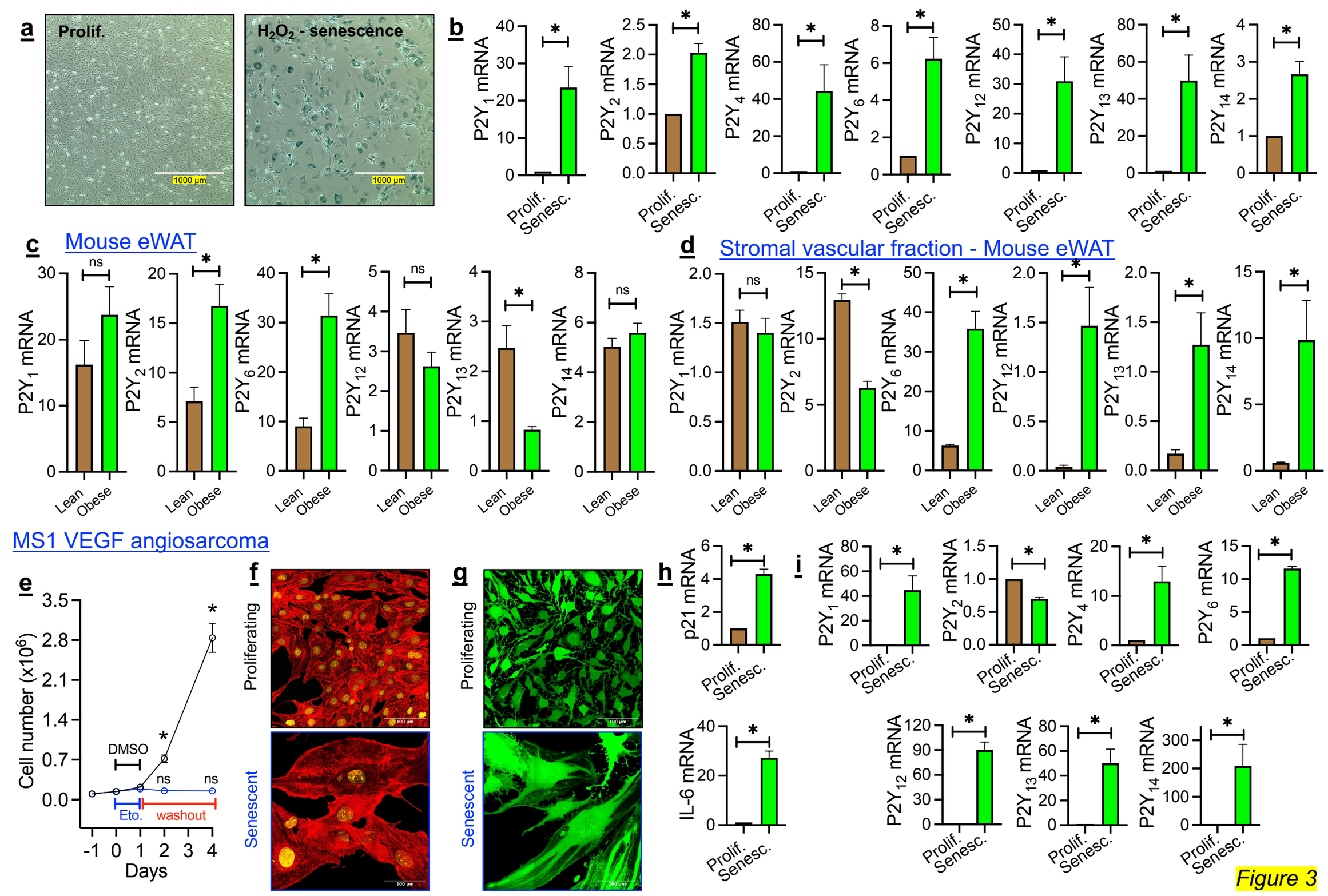
a
Prolif.
H_2O_2 - senescence
1000 µm
b
$P2Y_1$ mRNA
$P2Y_2$ mRNA
$P2Y_4$ mRNA
$P2Y_6$ mRNA
$P2Y_{12}$ mRNA
$P2Y_{13}$ mRNA
$P2Y_{14}$ mRNA
Prolif.
Senesc.
c
Mouse eWAT
ns
Lean
Obese
d
Stromal vascular fraction - Mouse eWAT
MS1 VEGF angiosarcoma
e
Cell number (x10^6)
DMSO
Eto.
washout
Days
f
Proliferating
Senescent
g
h
p21 mRNA
i
IL-6 mRNA

Figure 3

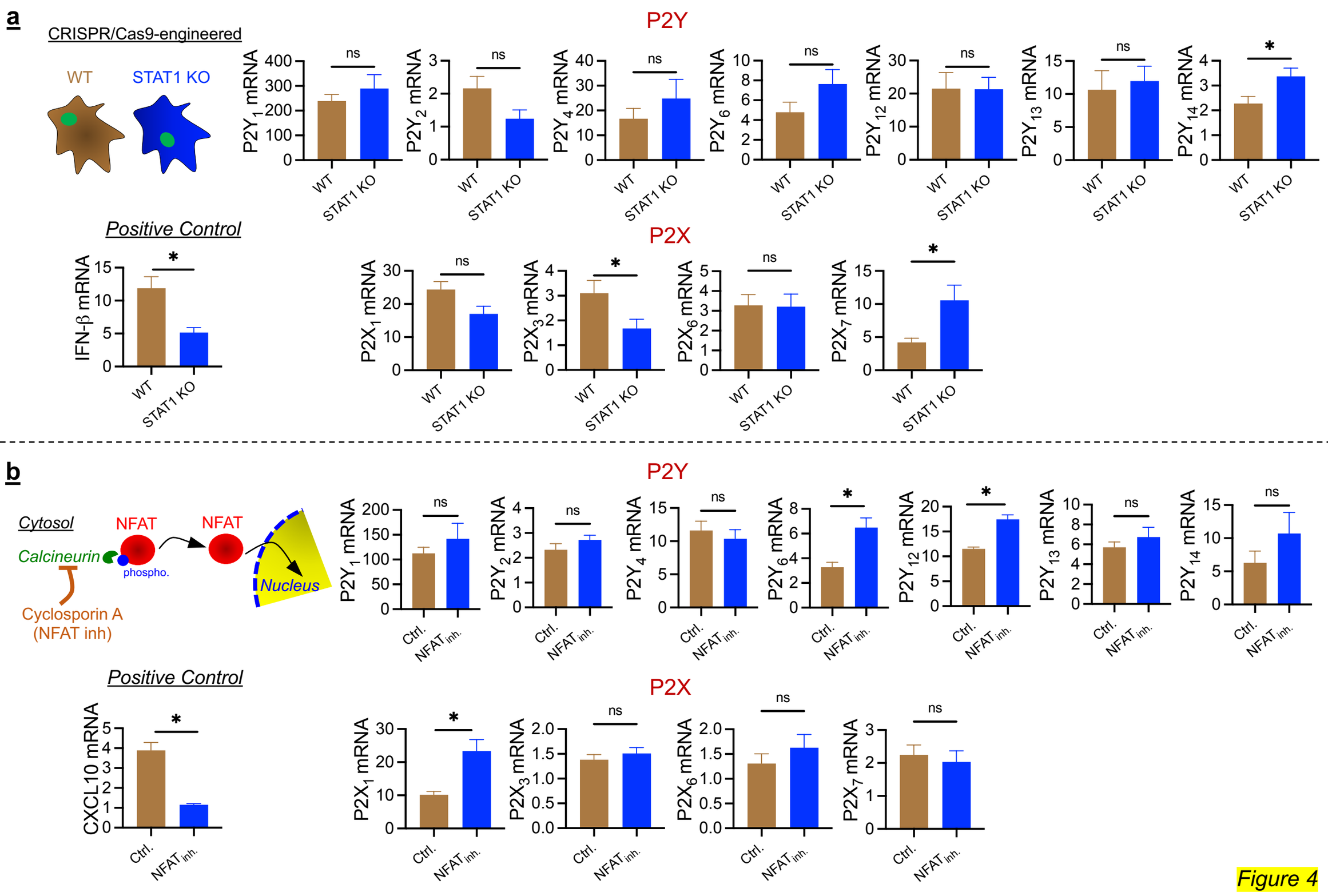
a
CRISPR/Cas9-engineered
WT
STAT1 KO
P2Y
P2Y1 mRNA
P2Y2 mRNA
P2Y4 mRNA
P2Y6 mRNA
P2Y12 mRNA
P2Y13 mRNA
P2Y14 mRNA
ns
*
WT
STAT1 KO
Positive Control
IFN-β mRNA
P2X
P2X1 mRNA
P2X3 mRNA
P2X6 mRNA
P2X7 mRNA
b
Cytosol
NFAT
Calcineurin
phospho.
Nucleus
Cyclosporin A
(NFAT inh)
Ctrl.
NFATinh.
CXCL10 mRNA
Figure 4

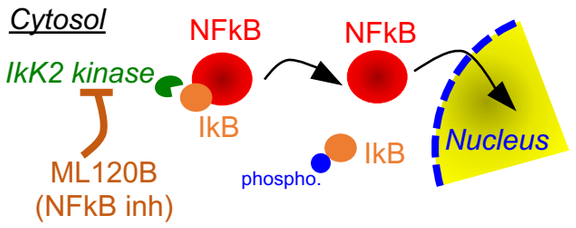

P2Y

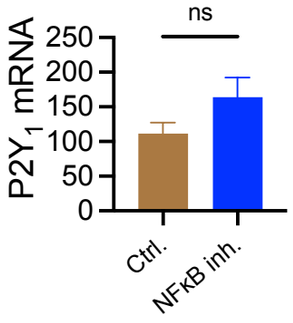

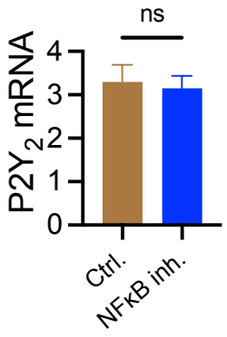

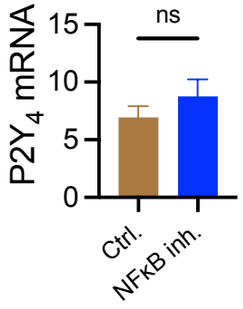

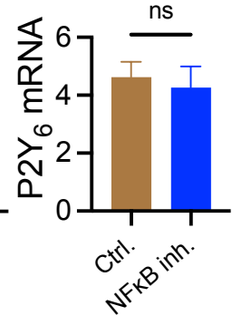

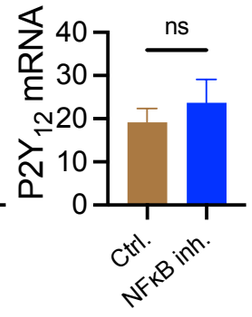

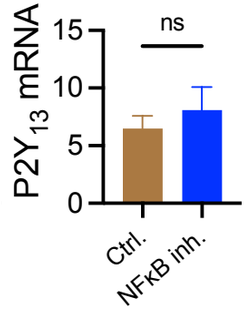

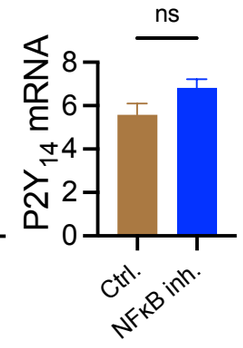

Positive Control

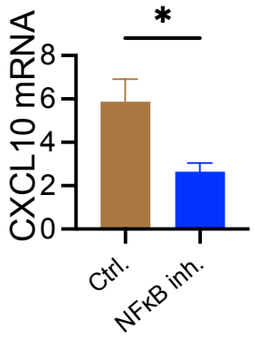

P2X

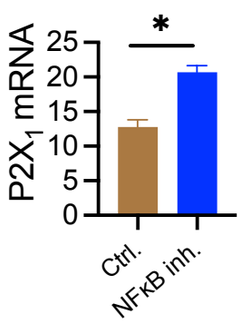

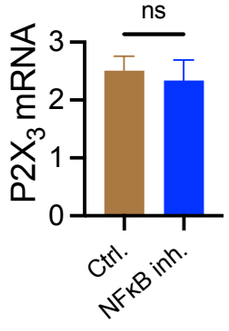

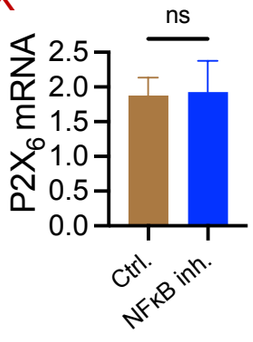

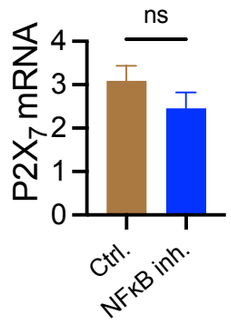

Figure 5

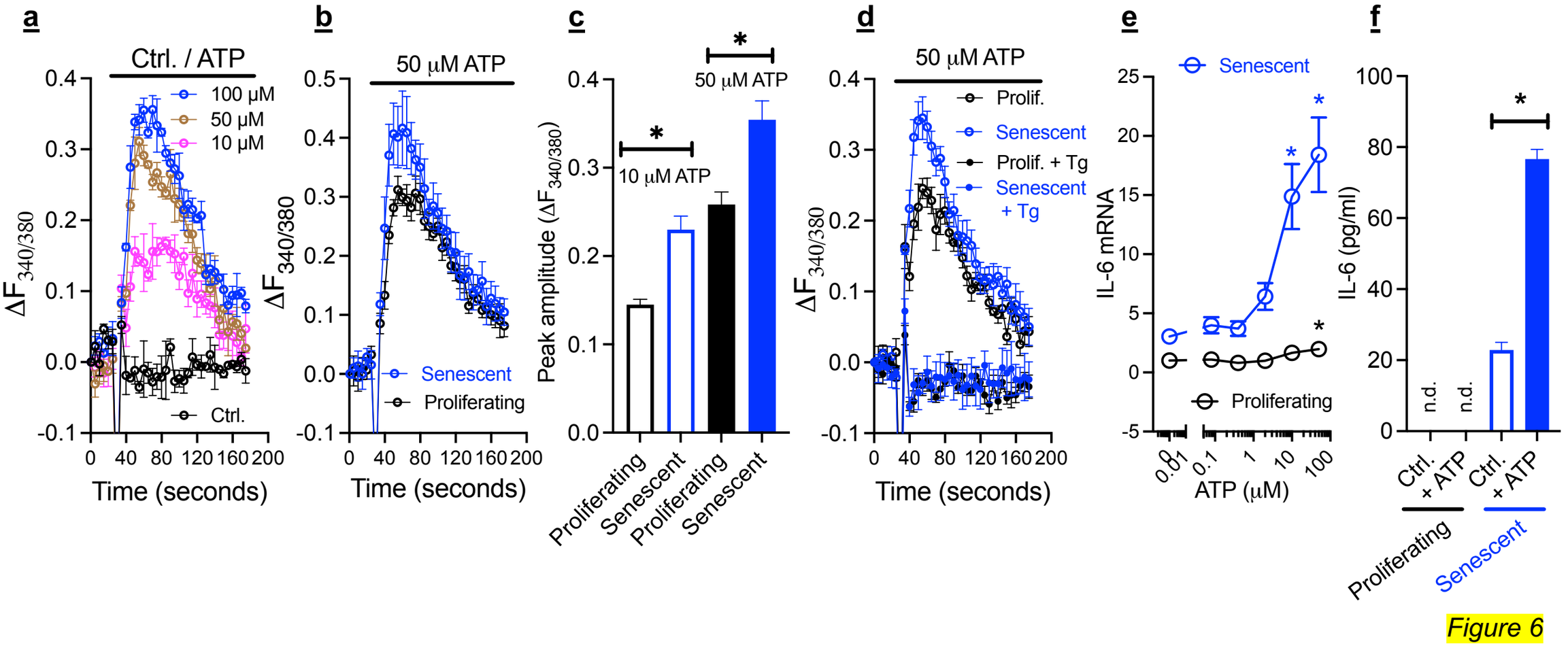
a
Ctrl. / ATP
100 μM
50 μM
10 μM
Ctrl.
ΔF340/380
Time (seconds)
b
50 μM ATP
Senescent
Proliferating
ΔF340/380
Time (seconds)
c
50 μM ATP
10 μM ATP
Peak amplitude (ΔF340/380)
Proliferating
Senescent
Proliferating
Senescent
d
50 μM ATP
Prolif.
Senescent
Prolif. + Tg
Senescent + Tg
ΔF340/380
Time (seconds)
e
Senescent
Proliferating
IL-6 mRNA
ATP (μM)
f
IL-6 (pg/ml)
n.d.
n.d.
Ctrl.
+ ATP
Ctrl.
+ ATP
Proliferating
Senescent

Figure 6

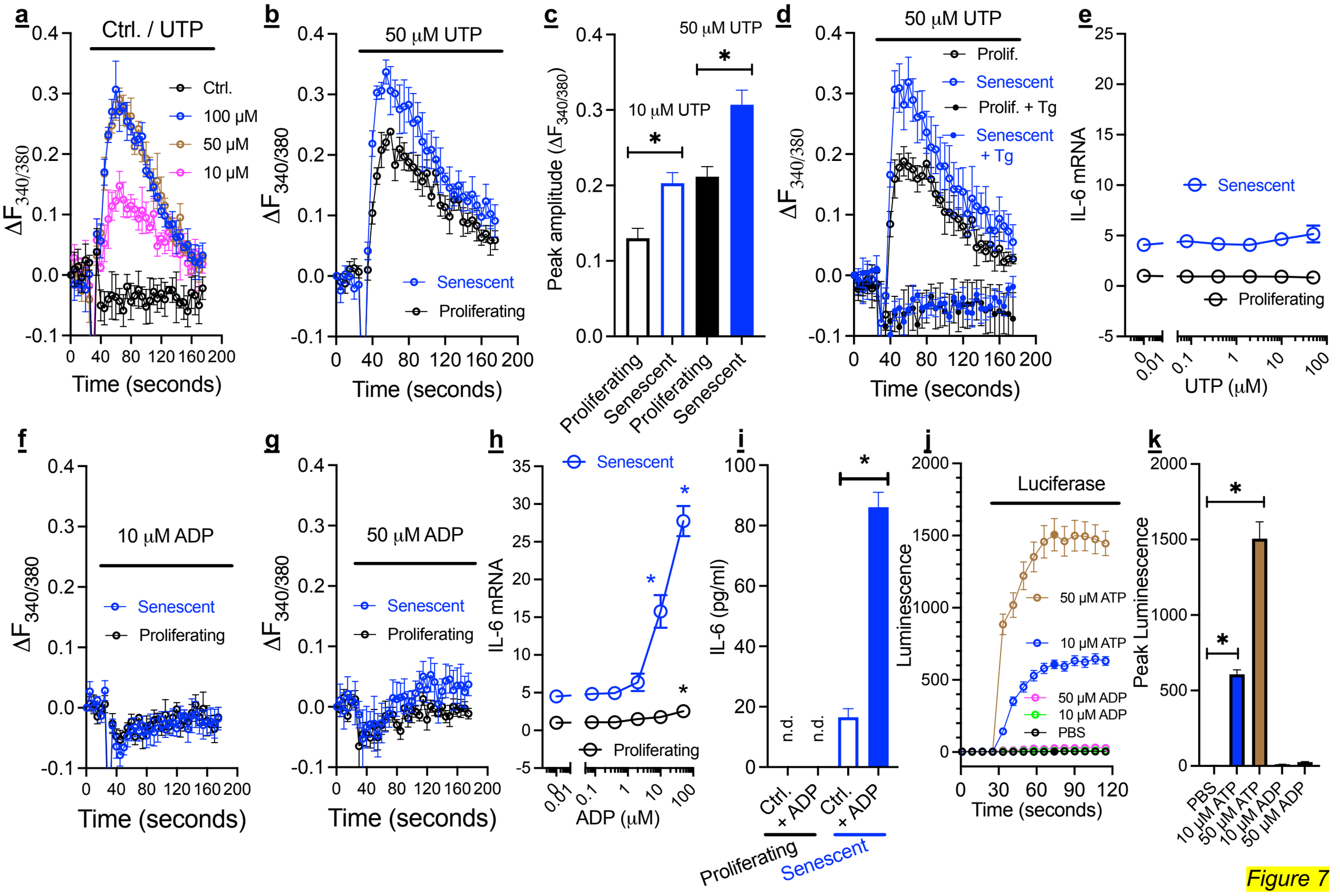
a
Ctrl. / UTP
Ctrl.
100 µM
50 µM
10 µM
ΔF340/380
Time (seconds)
b
50 µM UTP
Senescent
Proliferating
ΔF340/380
Time (seconds)
c
50 µM UTP
10 µM UTP
Peak amplitude (ΔF340/380)
Proliferating
Senescent
Proliferating
Senescent
d
50 µM UTP
Prolif.
Senescent
Prolif. + Tg
Senescent + Tg
ΔF340/380
Time (seconds)
e
Senescent
Proliferating
IL-6 mRNA
UTP (µM)
f
10 µM ADP
Senescent
Proliferating
ΔF340/380
Time (seconds)
g
50 µM ADP
Senescent
Proliferating
ΔF340/380
Time (seconds)
h
Senescent
Proliferating
IL-6 mRNA
ADP (µM)
i
IL-6 (pg/ml)
n.d.
n.d.
Ctrl.
+ ADP
Ctrl.
+ ADP
Proliferating
Senescent
j
Luciferase
50 µM ATP
10 µM ATP
50 µM ADP
10 µM ADP
PBS
Luminescence
Time (seconds)
k
Peak Luminescence
PBS
10 µM ATP
50 µM ATP
10 µM ADP
50 µM ADP

Figure 7

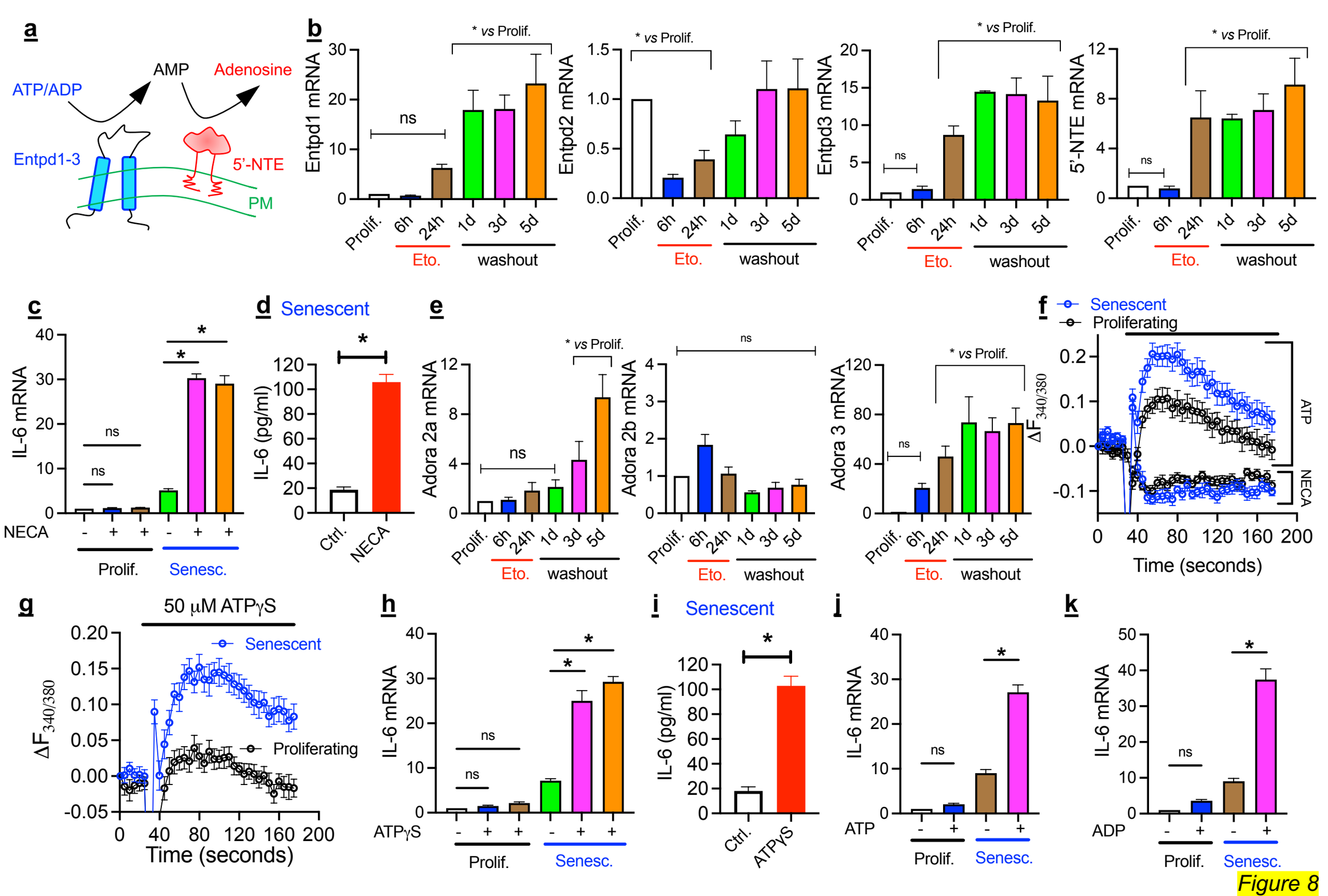
a
AMP
Adenosine
ATP/ADP
Entpd1-3
5'-NTE
PM
b
Entpd1 mRNA
Entpd2 mRNA
Entpd3 mRNA
5'-NTE mRNA
* vs Prolif.
ns
Prolif.
6h
24h
1d
3d
5d
Eto.
washout
c
IL-6 mRNA
NECA
Prolif.
Senesc.
d
Senescent
IL-6 (pg/ml)
Ctrl.
NECA
e
Adora 2a mRNA
Adora 2b mRNA
Adora 3 mRNA
f
Senescent
Proliferating
ΔF340/380
ATP
NECA
Time (seconds)
g
50 μM ATPγS
Senescent
Proliferating
ΔF340/380
Time (seconds)
h
IL-6 mRNA
ATPγS
Prolif.
Senesc.
i
Senescent
IL-6 (pg/ml)
Ctrl.
ATPγS
j
IL-6 mRNA
ATP
Prolif.
Senesc.
k
IL-6 mRNA
ADP
Prolif.
Senesc.

Figure 8

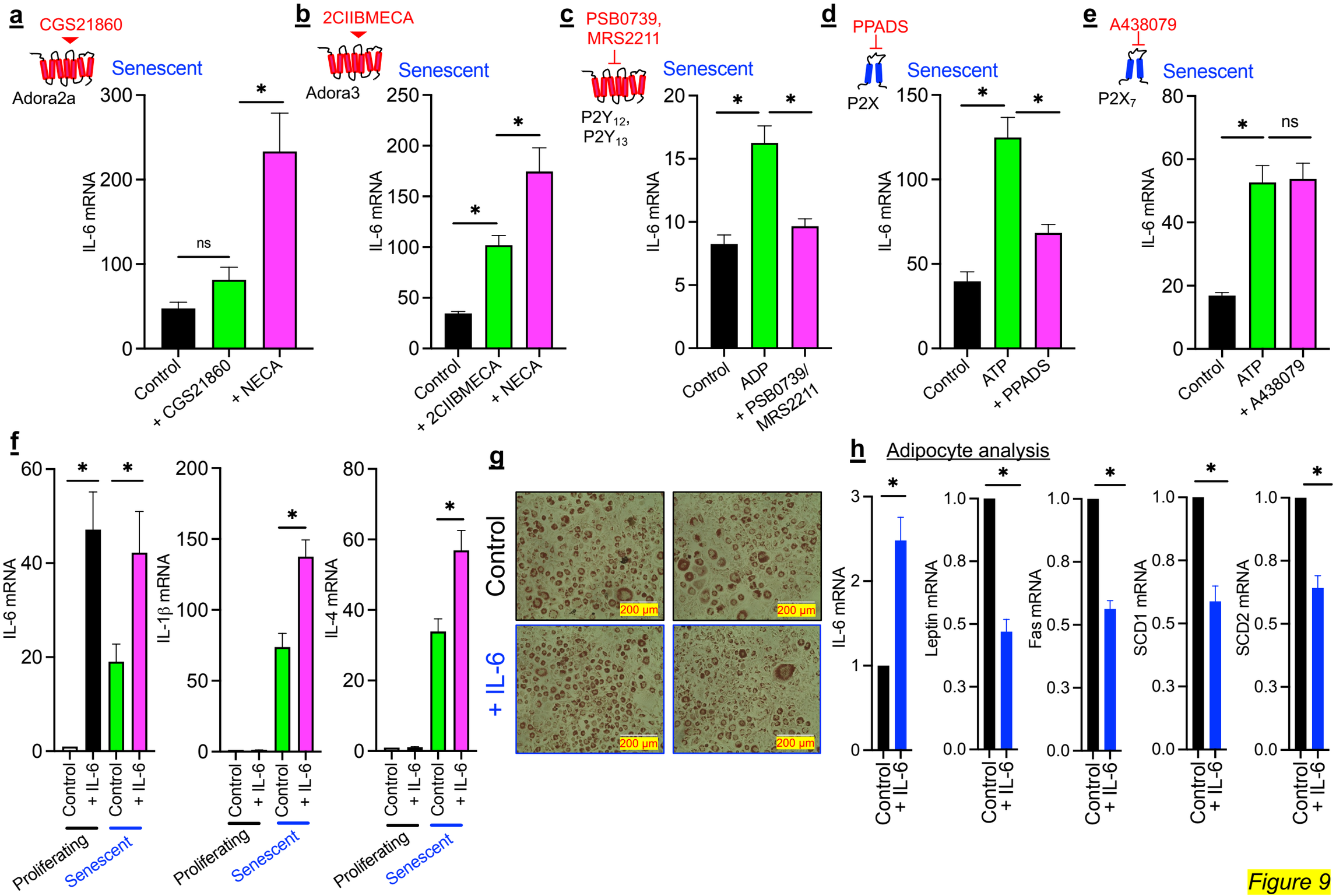
a
CGS21860
Adora2a
Senescent
IL-6 mRNA
300
200
100
0
*
ns
Control
+ CGS21860
+ NECA
b
2CIIBMECA
Adora3
Senescent
IL-6 mRNA
250
200
150
100
50
0
*
*
Control
+ 2CIIBMECA
+ NECA
c
PSB0739,
MRS2211
P2Y12,
P2Y13
Senescent
IL-6 mRNA
20
15
10
5
0
*
*
Control
ADP
+ PSB0739/
MRS2211
d
PPADS
P2X
Senescent
IL-6 mRNA
150
100
50
0
*
*
Control
ATP
+ PPADS
e
A438079
P2X7
Senescent
IL-6 mRNA
80
60
40
20
0
*
ns
Control
ATP
+ A438079
f
IL-6 mRNA
60
40
20
0
IL-1β mRNA
200
150
100
50
0
IL-4 mRNA
80
60
40
20
0
*
Control
+ IL-6
Proliferating
Senescent
g
Control
+ IL-6
200 µm
h
Adipocyte analysis
IL-6 mRNA
3
2
1
0
Leptin mRNA
1.0
0.8
0.5
0.3
0.0
Fas mRNA
SCD1 mRNA
SCD2 mRNA
*
Control
+ IL-6

Figure 9

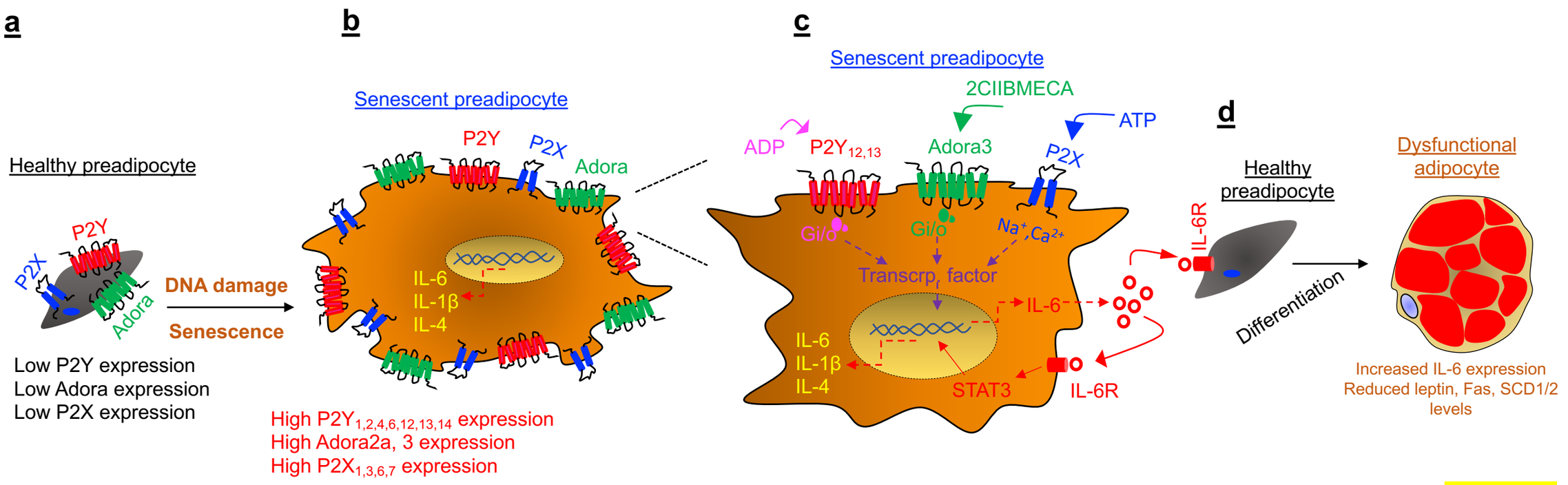
a
Healthy preadipocyte
P2Y
P2X
Adora
DNA damage
Senescence
Low P2Y expression
Low Adora expression
Low P2X expression
b
Senescent preadipocyte
P2Y
P2X
Adora
IL-6
IL-1β
IL-4
High P2Y1,2,4,6,12,13,14 expression
High Adora2a, 3 expression
High P2X1,3,6,7 expression
c
Senescent preadipocyte
2CIIBMECA
ATP
ADP
P2Y12,13
Adora3
P2X
Gi/o
Gi/o
Na+,Ca2+
Transcrp. factor
IL-6
IL-6
IL-1β
IL-4
STAT3
IL-6R
IL-6R
d
Healthy preadipocyte
Differentiation
Dysfunctional adipocyte
Increased IL-6 expression
Reduced leptin, Fas, SCD1/2 levels

Figure 10

Supplementary Data

STAT1- and NFAT-independent amplification of purinoceptor function integrates DNA damage-induced cellular senescence with interleukin-6 production in preadipocytes

Yasser Majeed[1], Aisha Y. Madani[1], Ahmed I. Altamimi[1], Raphael Courjaret[2], Muneera Vakayil[1,3], Samuel J. Fountain[4], Khaled Machaca[2], Nayef A. Mazloum[1, *]

[1]Department of Microbiology and Immunology, Weill Cornell Medicine-Qatar, Qatar Foundation, Doha, Qatar
[2]Department of Physiology and Biophysics, Weill Cornell Medicine-Qatar, Qatar Foundation, Doha, Qatar
[3]College of Health & Life Sciences, Hamad Bin Khalifa University, Qatar Foundation, Doha, Qatar
[4]School of Biological Sciences, University of East Anglia, Norwich, United Kingdom

*Corresponding author:

Nayef A. Mazloum (nam2016@qatar-med.cornell.edu)

Supplementary Figures

Supplementary Figure 1: (a) Representative images of DMSO or etoposide-treated (5 hours) preadipocytes stained with Hoechst and an antibody specific for histone H2AX phosphorylation at serine 139 (γH2AX). Scale bar, 50 μm. (b) Representative images of proliferating or senescent preadipocytes stained with DyLight™ Phalloidin 594 and Hoechst. Scale bar, 100 μm. (c) Representative images of proliferating or senescent preadipocytes stained with Calcein-AM. Scale bar, 100 μm. (d) qPCR Ct values for the indicated interleukin (IL) genes and the housekeeping reference gene Ribosomal Protein Lateral Stalk Subunit P0 (RPLP0). Etoposide-exposure (Eto.) and washout durations are indicated in hours (h) and days (d), respectively. These numbers were used to calculate fold-change values shown in Figure 1.

Supplementary Figure 2: (a, b) qPCR Ct values for the indicated P2Y and P2X genes. Etoposide-exposure (Eto.) and washout durations are indicated in hours (h) and days (d), respectively. These numbers were used to calculate fold-change values shown in Figure 2.

Supplementary Figure 3: (a) P2Y receptor expression analysis carried out in liver tissues isolated from lean or obese mice (n=6). (b, c) Representative images of proliferating or senescent MS1 VEGF angiosarcoma cells stained with DyLight™ Phalloidin 594 and Hoechst (b) or with Calcein-AM (c).

Supplementary Figure 4: qPCR data showing changes in the expression levels of the indicated genes in proliferating or Etoposide-treated control (WT) or STAT1 knockout (KO) 3T3-L1 preadipocytes (n=6). STAT1 KO preadipocytes were generated using CRISPR/Cas9 technology as previously described (see methods). Statistical analysis was performed using Kruskal-Wallis test with post-hoc Dunn's test.

Supplementary Figure 5: qPCR data showing changes in the expression levels of the indicated genes in proliferating or etoposide-treated preadipocytes exposed to solvent (Control, DMSO) or 5 µg/ml cyclosporin A (NFAT inh.) (n=6). Statistical analysis was performed using Kruskal-Wallis test with post-hoc Dunn's test.

Supplementary Figure 6: qPCR data showing changes in the expression levels of the indicated genes in proliferating or etoposide-treated preadipocytes exposed to solvent (Control, DMSO) or 10 µM ML120B (NFkB inh.) (n=6). Statistical analysis was performed using Kruskal-Wallis test with post-hoc Dunn's test.

Supplementary Figure 7: (a, b) qPCR Ct values for the indicated Entpd and Adora genes. Etoposide-exposure (Eto.) and washout durations are indicated in hours (h) and days (d), respectively. These numbers were used to calculate fold-change values shown in Figure 7.

Supplementary Tables

Supplementary Table 1: Sequences of the gene-specific primers used in this study.

TARGET NAME	FORWARD PRIMER (5'-3')	REVERSE PRIMER (5'-3')
MOUSE		
P2Y1	GAGGTGCCTTGGTCGGTTG	CGGCAGGTAGTAGAACTGGAA
P2Y2	CTGGAACCCTGGAATAGCACC	CACACCACGCCATAGGACA
P2Y4	ATGACCAGTGCAGACTCCTTG	GAGGCAACAGGATGAACTTGA
P2Y6	GTGAGGATTTCAAGCGACTGC	TCCCCTCTGGCGTAGTTATAGA
P2Y12	CCCTGTGCGTCAGAGACTAC	CAAGCTGTTCGTGATGAGCC
P2Y13	ATGCTCGGGACAATCAACACC	GATGTGGACGAACACCCAGAG
P2Y14	TGGCACAAGGCGTCTAACTAT	GACTTCCTCTTGACGGAGGTG
P2X1	AGATGACAGTGGCTGCACTC	TGAAGAAGAGCAGGGCTTGG
P2X2	TGGACAGGCAGGGAAATTCA	AGGCCATCTACTTGAGGGGT
P2X3	GGTGGCTGTGAGCACTTTCT	GCAAGAAAACCCACCCCACA
P2X4	GCTTACGTCATTGGGTGGGT	AAGTGTTGGTCACAGCCACA
P2X5	CCCACTGCAACCCACACTAT	TTCCCGCCTTGCCATTAACT
P2X6	CAGCCATGGCATAAAAACTGGT	TTCTTGGCCTGAGCTAGCAG
P2X7	TGTAAGTGCTGTGAGCCCTG	AGTCCATCTGGGGTCTTGGA
IL-1β	GCCACCTTTTGACAGTGATGAG	TGATACTGCCTGCCTGAAGC
IL-2	TCTGCGGCATGTTCTGGATT	TGTGTTGTCAGAGCCCTTTAGT

IL-4	TCCTCACAGCAACGAAGAACA	AGGCATCGAAAAGCCCGAAA
IL-5	ATGAGGCTTCCTGTCCCTACT	CGCCACACTTCTCTTTTTGGC
IL-6	CTGCAAGAGACTTCCATCCAG	AGTGGTATAGACAGGTCTGTTGG
ENTPD1	TACGAACAGTGCCACCAGAG	GAAAGCAGAAAACGCCCCAA
ENTPD2	ATGCGCCTACTCAACCTGAC	AGCAGGTAGTTGGCAGTCAC
ENTPD3	ACGGTGCAGGTGTCTCTGTA	TTCCGTGGAAGGGCTCTGTA
IFNβ	CCTGGAGCAGCTGAATGGAA	CCACCCAGTGCTGGAGAAAT
ADORA 2A	ATTCGCCATCACCATCAGCA	AAGCCATTGTACCGGAGTGG
ADORA 2B	CGTCCCGCTCAGGTATAAAG	GTCACAGGACAGCAGCTTTT
ADORA 3	GGATTTGGCTGCAGAGACCT	ACTTGCTCATTCCTTCCGGT
5'-NTE	TCCTGCAAGTGGGTGGAATC	AGATGGGCACTCGACACTTG
CXCL10	CCAAGTGCTGCCGTCATTTTC	GGCTCGCAGGGATGATTTCAA
RPLP0	AACCCTGAAGTGCTCGACAT	GAAGGCCTTGACCTTTTCAGT
LEPTIN	CAGCTGCAAGGTGCAAGAAG	GATACCGACTGCGTGTGTGA
SCD1	CAGGTTTCCAAGCGCAGTTC	GAACTGGAGATCTCTTGGAGCA
SCD2	GAGCAGATGTTCGCCCTGAA	ACAAATACGCGAAGAGACAGGT
FAS	GGAGGTGGTGATAGCCGGTAT	TGGGTAATCCATAGAGCCCAG

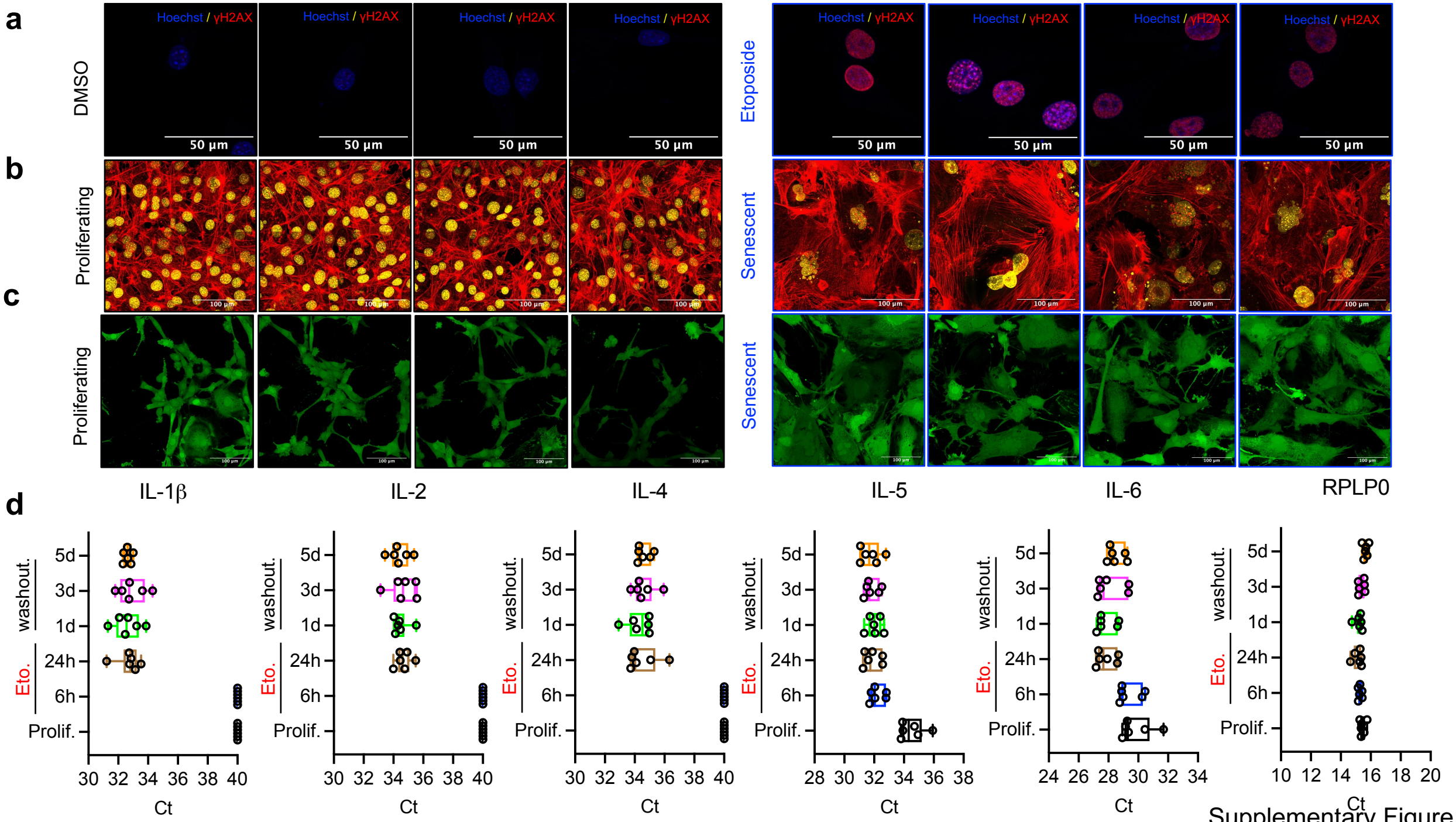

Supplementary Figure 1

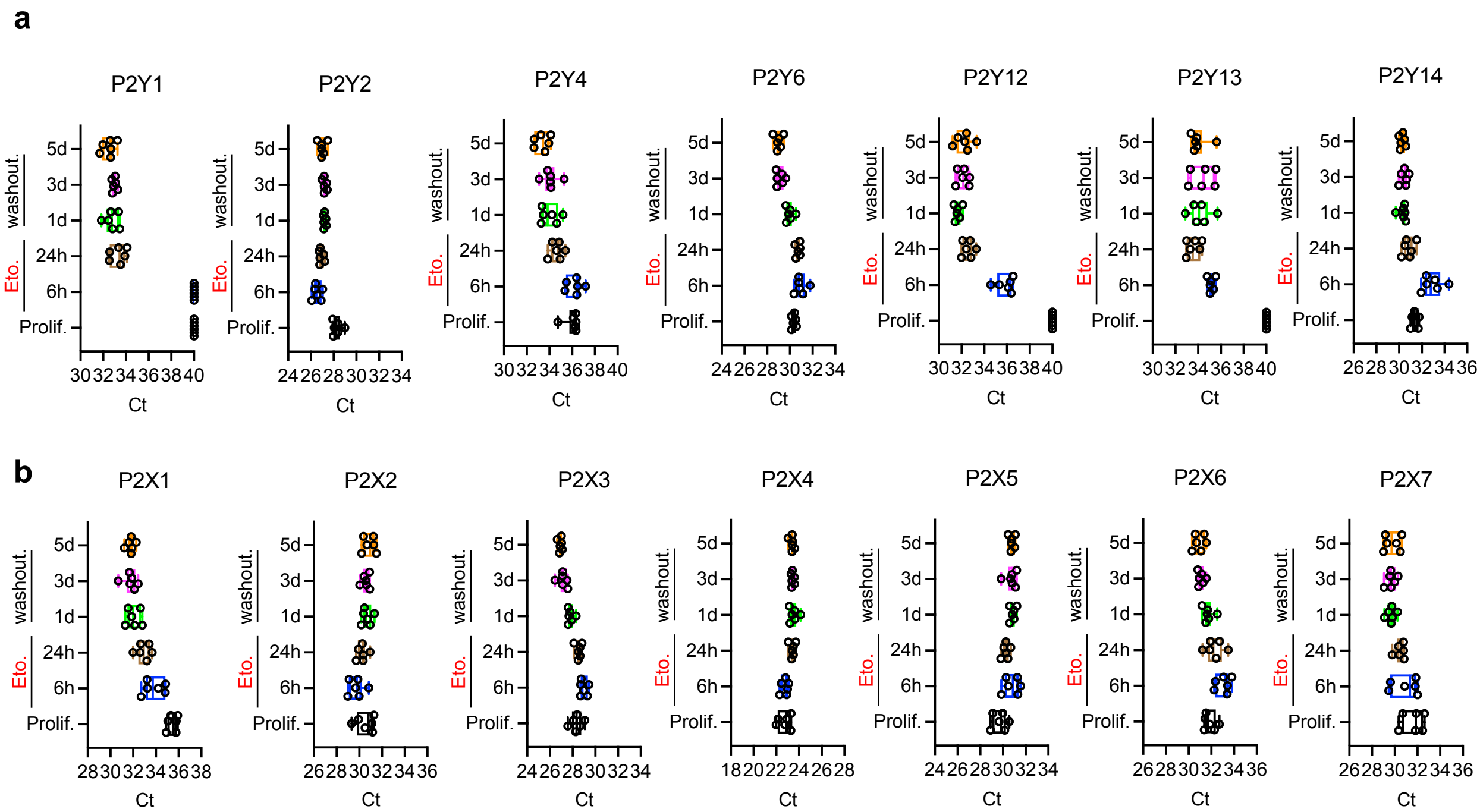

Supplementary Figure 2

a. Mouse liver tissue

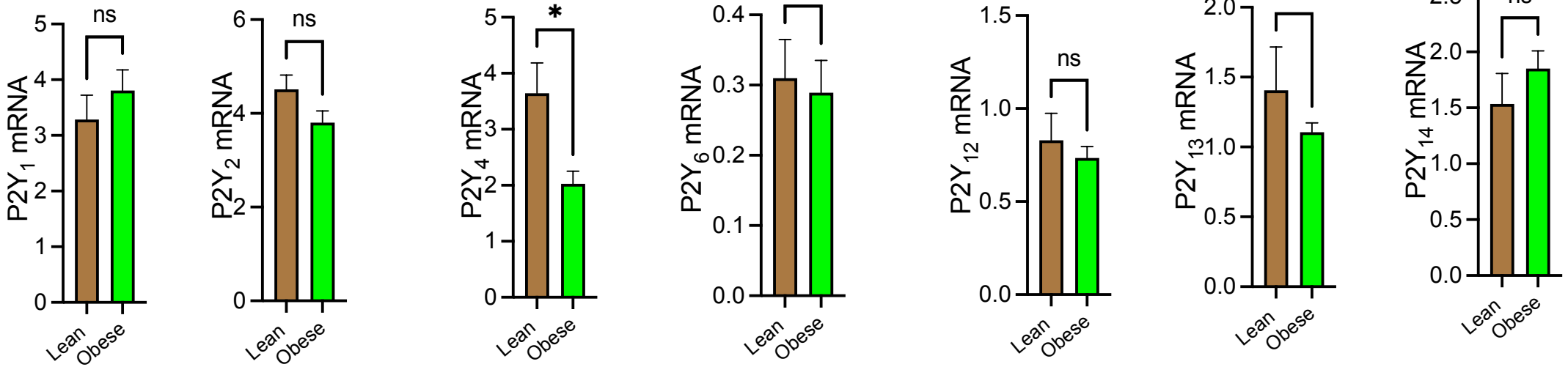

b. MS1 VEGF angiosarcoma cells - Phalloidin

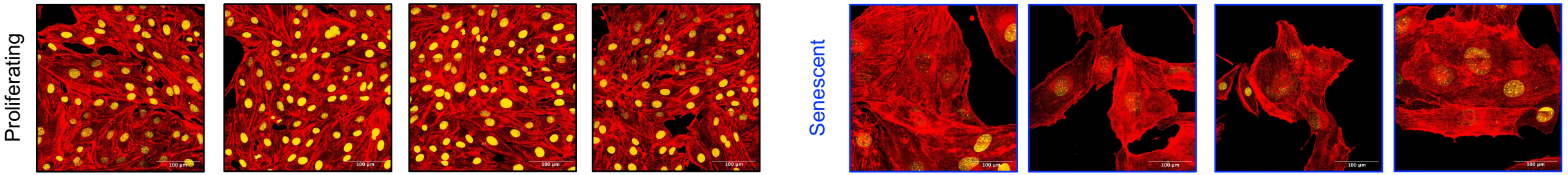

c. MS1 VEGF angiosarcoma cells – Calcein-AM

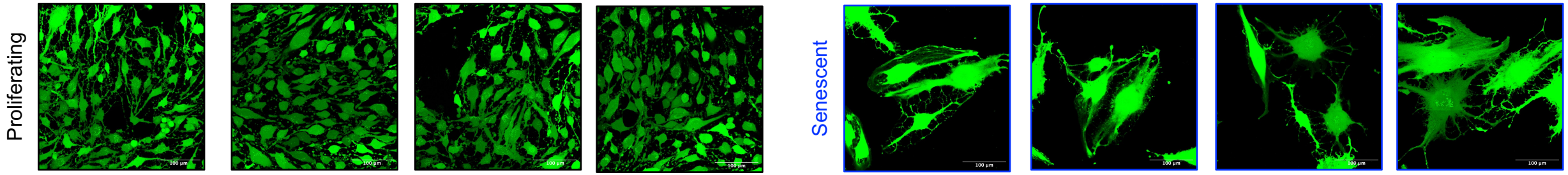

Supplementary Figure 3

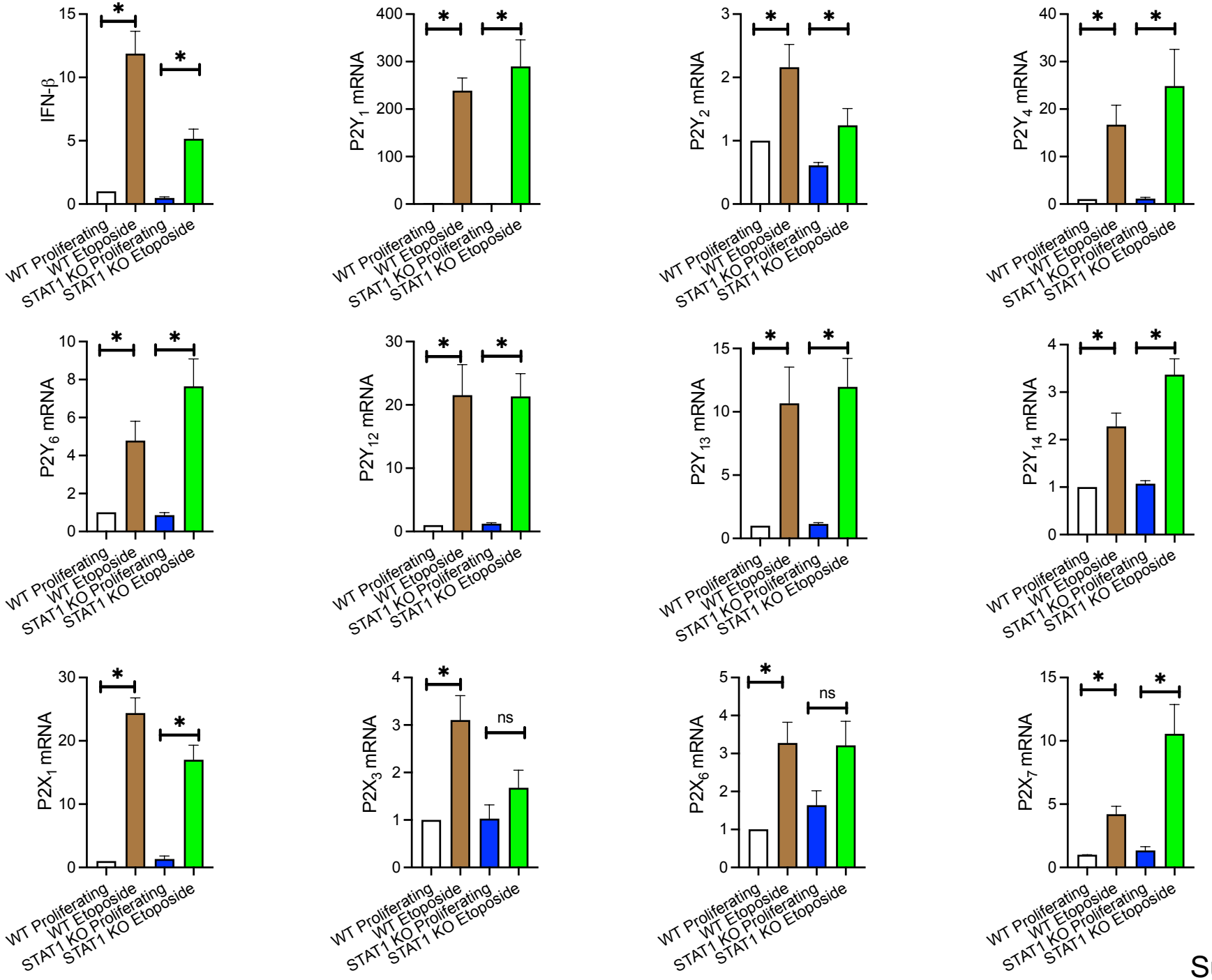

Supplementary Figure 4

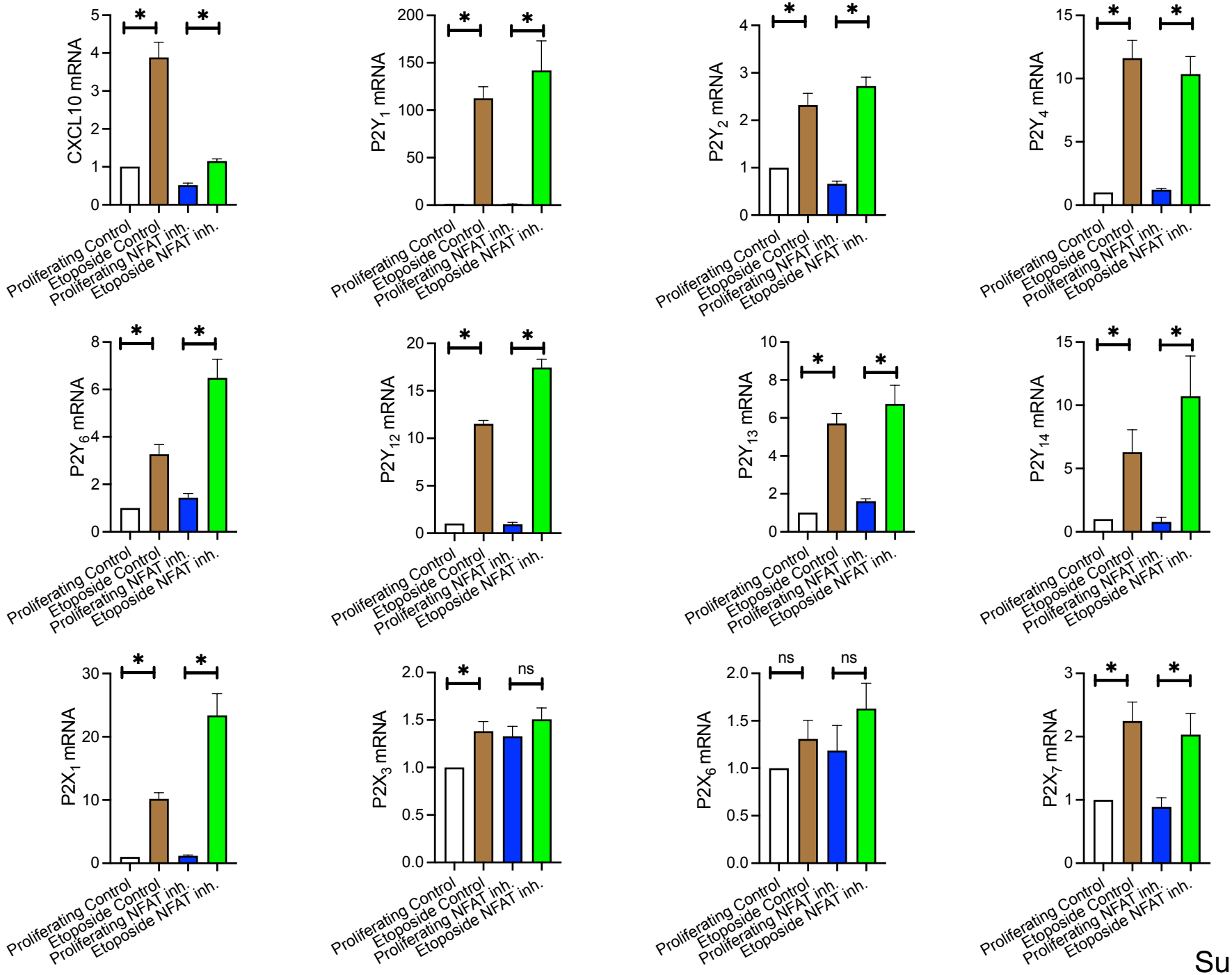

Supplementary Figure 5

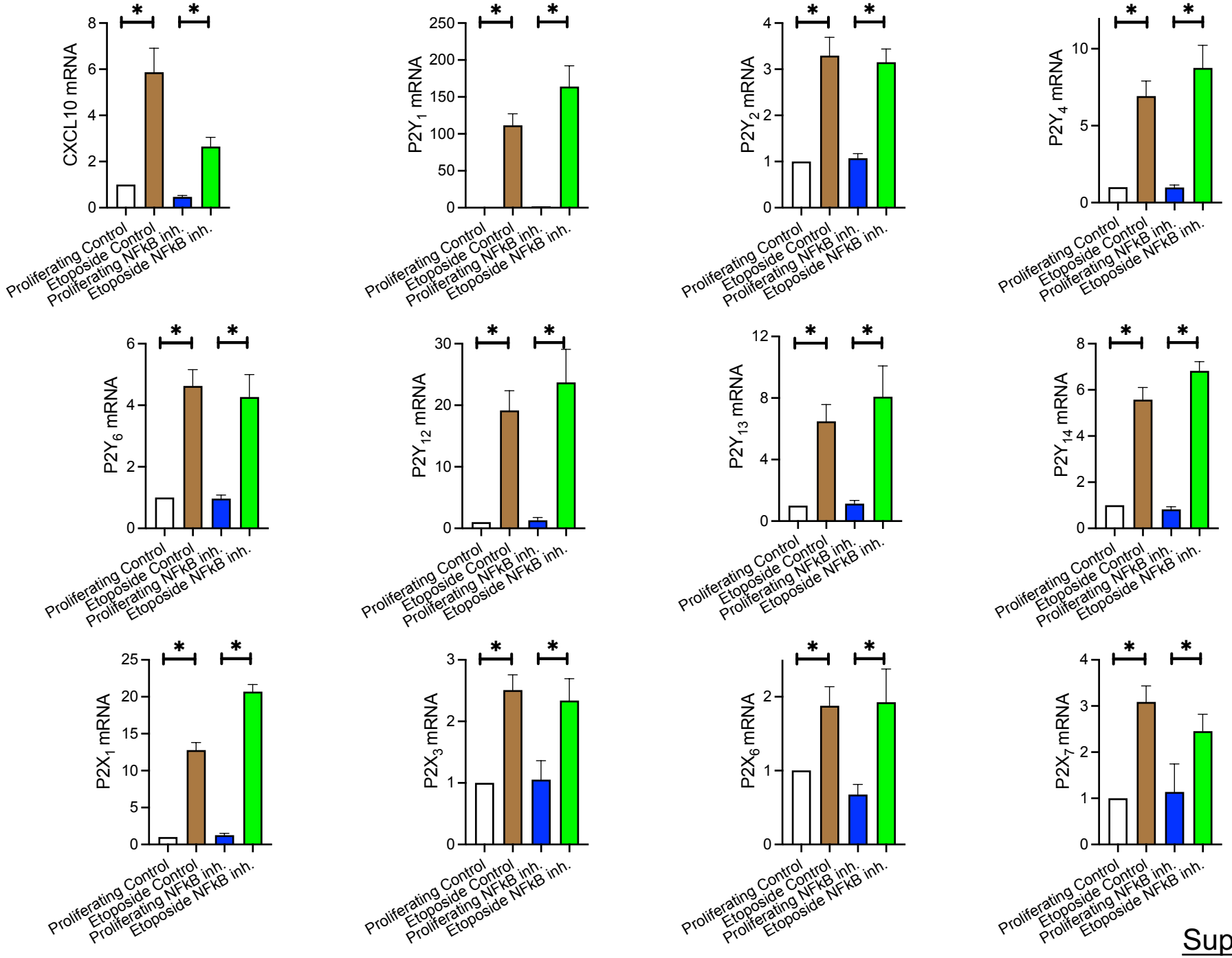

Supplementary Figure 6

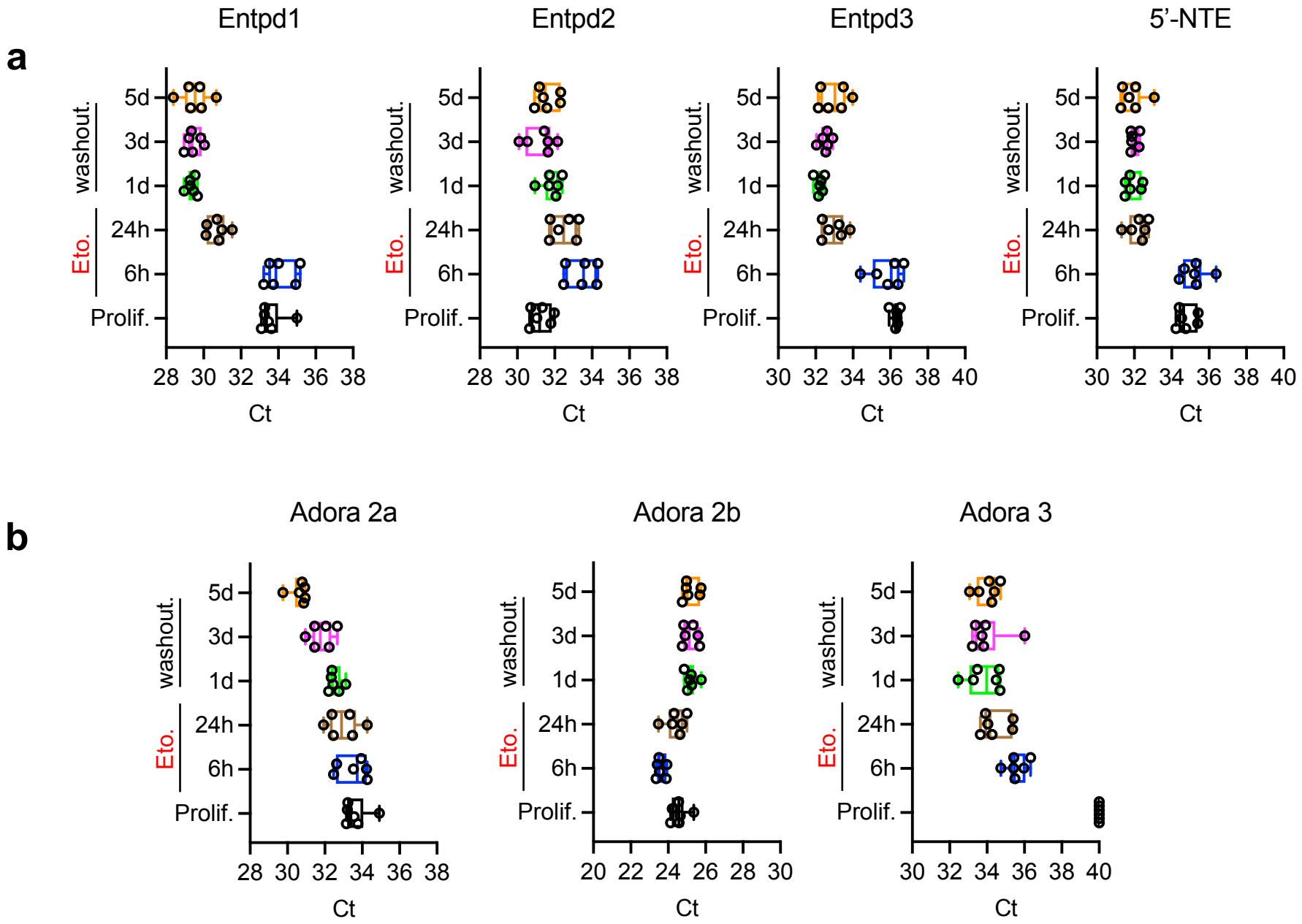

Supplementary Figure 7